An updated geothermal model of the Dutch subsurface based on inversion of temperature data

Eszter Békési, Maartje Struijk, Damien Bonté, Hans Veldkamp, Jon Limberger, Peter Fokker, Mark Vrijlandt, Jan-Diederik van Wees

1   An updated geothermal model of the Dutch subsurface based on inversion of temperature data

2   Eszter Békési,[1] Maartje Struijk[2], Damien Bonté[1,3], Hans Veldkamp[2], Jon Limberger[1,2], Peter A. Fokker[1,2], Mark
3   Vrijlandt[2], and Jan-Diederik van Wees[1,2]

4   [1]Department of Earth Sciences, Utrecht University, Utrecht 3584 CB, Netherlands.
5   [2] TNO Utrecht, Utrecht 3584 CB, Netherlands.
6   [3] IFP Energies Nouvelles, 1 et 4 avenue de Bois-Préau, 92852 Rueil-Malmaison, France.

7   Corresponding author: e.bekesi@uu.nl, Department of Earth Sciences, Tectonics Group, Utrecht University,
8   Princetonlaan 4, 3584 CB Utrecht

9   Highlights

10   • 3D subsurface thermal model of the onshore Netherlands
11   • Conductive heat transport
12   • Pseudo-convective approach to approximate hydrothermal convection
13   • Data assimilation using temperature measurements as observations

14

15   Abstract

16   The subsurface temperature is one of the most crucial parameters for the development of geothermal energy.
17   Physics-based temperature models calibrated with temperature data are especially relevant for deep geothermal
18   exploration. We present an updated high-resolution 3D thermal model of the onshore Netherlands. We
19   constructed the model in 7 steps, starting from a lithospheric-scale, physics-based forward model and
20   progressively detailing and updating it using temperature data. The model is built up from 14 sedimentary layers
21   and layers for the upper crust, lower crust, and lithospheric mantle. We assigned a-priori thermal properties for
22   each layer and updated them through an inversion procedure by the Ensemble Smoother with Multiple Data
23   Assimilation (ES-MDA), using 1507 temperature measurements as observations. Misfits of the prior model are
24   significantly reduced through the data assimilation procedure, demonstrating the effectiveness of ES-MDA as a
25   tool for calibrating temperature models, supporting high-resolution external constraints. The resulting posterior
26   model describes the thermal state in the uppermost 10 km of the Netherlands with a horizontal resolution of 1
27   km, a vertical resolution of 200 m, and an overall RMS misfit of 0.7 °C.

28   The thermal state of the deep subsurface is important for geothermal exploration that targets the deeply buried
29   Devonian-Carboniferous carbonate formations in the Netherlands. These reservoirs are potentially suitable for
30   industrial heating applications and electricity production. To this end, one of the main aspects of this study was
31   to incorporate the thermal effect of hydrothermal convection within the Dinantian carbonate platforms, following
32   the example found in the Luttelgeest-01 (LTG-01) well. Our model reveals areas in the Netherlands with
33   potential for convection in these carbonate platforms, highlighting locations that can be suitable for deep
34   geothermal development.

35

36   Keywords

37   3D thermal field, regional-scale conductive model, pseudo-convection, data assimilation, the Netherlands

38

39   1.   Introduction

40   Due to the increasing global energy demand, the shortage of conventional energy sources, and environmental
41   aspects, the exploitation of renewable energy sources are gaining importance quickly. Geothermal energy is a
42   good alternative to non-renewable energy sources, but geothermal energy systems need to satisfy several
43   constraints to become economic. The key parameters of geothermal systems are the reservoir temperature and
44   the fluid flow rate. The latter is strongly dependent on the reservoir permeability that should be sufficiently high
45   to support the flow rate and on the reservoir thickness. Alternatively, favorable reservoir conditions should be
46   present to allow for enhancement of the permeability (e.g. Enhanced Geothermal Systems (Breede et al., 2013)).
47   To assess potential areas for geothermal exploration, large-scale physics-based models integrating geophysics,

geology, and geochemistry are required (e.g. Cloetingh et al., 2010). However, for the development of a geothermal project, detailed site-specific studies are indispensable in order to minimize the pre-drilling risks associated with uncertainties in the subsurface.

In this paper we present a 3D thermal model of the onshore Netherlands. We describe the thermal state of the subsurface in order to identify thermal anomalies within the basins and basement, highlighting potential areas for geothermal development. Geothermal resources in the Netherlands can be classified as conduction dominated intracratonic basin plays (Moeck and Beardsmore, 2014). Geothermal projects focus on direct heat uses, targeting formations restricted to 2-3 km depth. At those depths, the average geothermal gradient of ~31°C/km prohibits electricity production, since sufficiently high temperatures are only reached at larger depth, below 4-5 km. For clastic reservoirs in the Netherlands, permeability at 4-5 km depth is not high enough for geothermal exploitation. The only exception, could be the Dinantian carbonate platforms with their natural fracture networks. Typically, deep geothermal projects in low to medium enthalpy reservoirs are mostly exploiting granite or sandstone reservoirs. However, in the Netherlands the focus is on the fractured carbonate platforms. The 4-km deep Luttelgeest carbonate platform drilled by the LTG-01 well, shows evidence for the presence of hydrothermal convection (Bonté et al., 2012; Lipsey et al., 2016; Van Oversteeg et al., 2014). Higher than average temperatures and the presence of fluids provide favorable conditions for deep geothermal exploitation. Therefore, one of the main aspects of the present study is to identify possible locations where convection in these carbonate platforms might occur and that currently lack temperature measurements.

Investigation of the subsurface temperature distribution in the Netherlands has been carried out for several decades. The first temperature maps of the Dutch subsurface are reported in the Atlas of subsurface temperatures in the European Community (Haenel, 1980), although the temperature dataset used to construct these maps is not available. In the update of the geothermal atlas (Haenel and Staroste, 1988) a temperature dataset of the Netherlands including measurements from 388 wells is reported. A larger dataset containing 334 bottom hole temperatures (BHT) and 53 drill stem tests (DST) is available in the third edition of the geothermal atlas (Hurtig et al., 1992). The majority of measurements are obtained from the uppermost 3 km of the subsurface, except two values at 5 km depth. Temperature maps in the atlas are only available at European scale and are constructed based on the extrapolation of measured values from shallower depth. Temperature measurements from 464 wells were incorporated into the latest geothermal atlas (Hurter and Haenel, 2002). The maps for the Netherlands in this latter atlas were constructed by Rijkers and Van Doorn (1997) who updated the maps published in older versions of the atlases for the Lower Triassic and the Lower Cretaceous formations that have geothermal potential. The temperature maps were generated by kriging, showing significant improvements. Large-scale temperature models for Europe including the Netherlands, calibrated with a compilation of temperature models based on measurements were also constructed by Limberger et al. (2014; 2018). Verweij (2003) further characterized the temperature distribution in the onshore Netherlands using not only temperature measurements but also a physics-based approach, taking into account calculated estimates of the thermal conductivity and heatflow of the main lithostratigraphical units. Since then the onshore temperature dataset of the Netherlands has been continuously updated (e.g Bonté et al., 2012; Boxem, 2010). The first 3D temperature model of the onshore Netherlands has been constructed by Bonté et al. (2012). Here we present an update of their work using the most recent temperature data, an updated geological model and a significantly improved inverse modeling approach.

We modeled the thermal field of the deep subsurface of the Netherlands in 7 steps. We first constructed a physics-based lithospheric-scale thermal model, hereafter referred to as prior model. The resulting thermal model shows a misfit with the observed temperatures, highlighting areas where the steady-state conductive thermal field is perturbed by transient effects and/or convective heat transport (i.e. paleo-temperature fluctuations, groundwater flow). This misfit is reduced with sequential data-assimilation and more detailed modeling procedures, by updating the thermal properties of the layers using ES-MDA (Emerick and Reynolds, 2013a). Ensemble methods such as the Ensemble-Kalman Filter (EnKF) and the Ensemble Smoother (ES) are applicable for large problems having many parameters. Emerick and Reynolds (2013b) showed that in case of non-linear problems, ES-MDA performs better and is computationally more efficient than EnKF. ES-MDA is most commonly applied for history matching in reservoir modeling. For instance, Fokker et al. (2016) constrained the model parameters of a compacting gas field in the Netherlands with ES-MDA using satellite data. Inversion using ES-MDA to calibrate temperature models was previously applied by Békési et al. (2017) and Limberger et al. (2018). We followed a similar methodology by applying the ES-MDA to constrain the thermal conductivity of the sedimentary units and heat generation in the upper crust. This work flow yielded our final thermal model hereafter referred to as posterior model, describing the thermal state of the uppermost 10 km of the Dutch subsurface.

2. Geology and geothermal conditions

104 The geological structure of the sedimentary cover of the Netherlands was described in detail by Kombrink et al.
105 (2012) (Figure 1). A high resolution 2.5D model (DGM-deep v4.0) representing the main sedimentary units to
106 the base of the Carboniferous, reaching a depth up to 3-4 km in most of the country, is available from the
107 Netherlands Oil and Gas Portal website (www.nlog.nl). A cross section is presented in Figure 2. Detailed
108 descriptions of the units are available from the www.dinoloket.nl website (Van Adrichem Boogaert and Kouwe,
109 1993). Units of Devonian, Silurian and Ordovician and older age have seldomly been drilled onshore. The
110 descriptions of those units in the Dutch stratigraphic nomenclator are therefore incomplete and limited due to the
111 lack of data available. . The pre-Variscan basement is unknown in the Netherlands itself, but is considered to
112 consist of Avalonian crust (Pharaoh et al., 2010), which forms the core of the London Brabant Massif south of
113 the Netherlands. Wong et al. (2007) provide a concise description of the Devonian and younger rocks in the
114 Netherlands. Below, only a short description is given, largely based on Wong et al. (2007), Kombrink et al.
115 (2012), Bonté et al. (2012) and Smit et al. (2018).

116
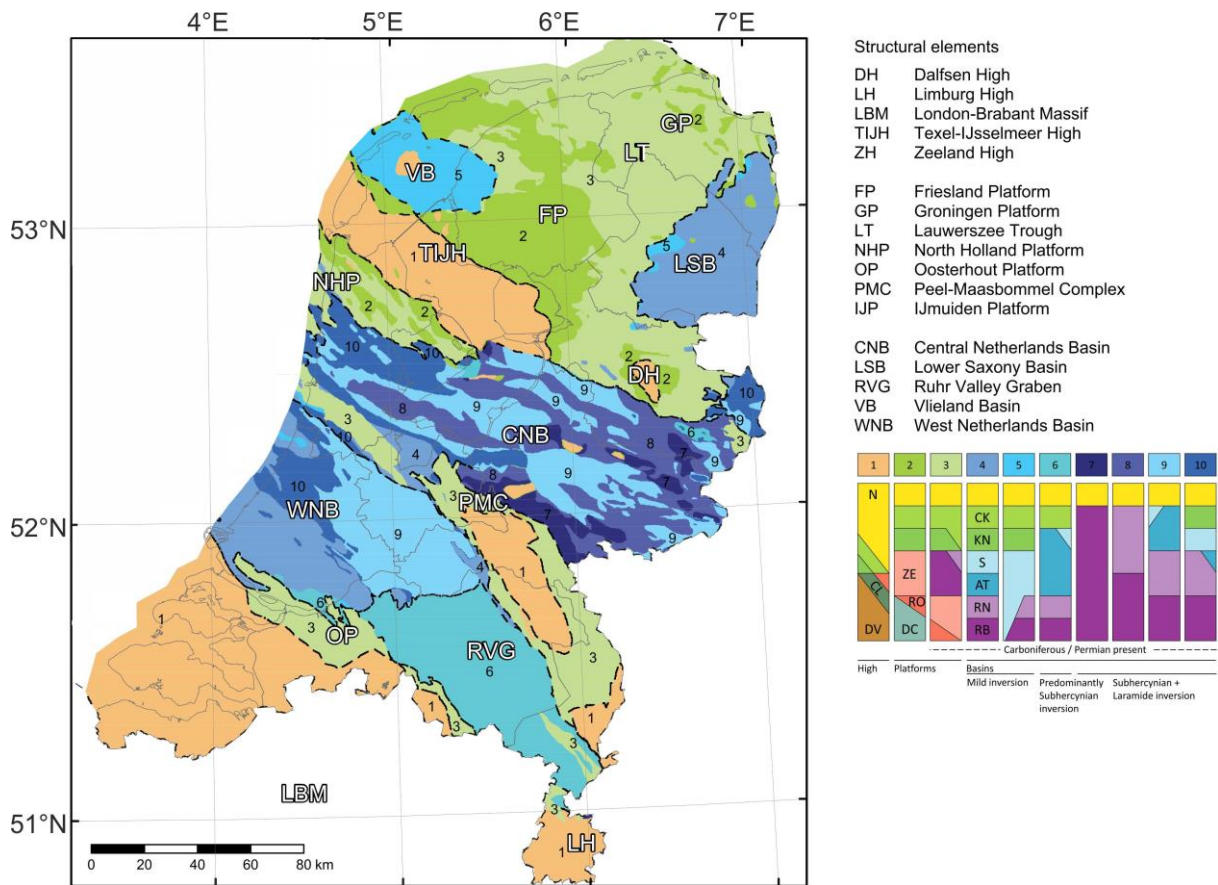
118 *Figure 1. Early Carboniferous - Late Jurassic structural elements of the Netherlands. The colour coding reflects*
119 *the remaining sedimentary succession. Areas that have been relatively stable in green and orange, inverted*
120 *basins in blue (after Kombrink et al., 2012).*

121

122 In the Devonian and Carboniferous, lithospheric stretching and subsidence associated with the Variscan orogeny
123 enabled the deposition in the Devonian of sandstones and shales in the southern Netherlands (Kombrink, 2008)
124 and reefal limestones in the north (Van Hulten and Poty, 2008). During the Early Carboniferous carbonate ramps
125 in the south, and isolated platforms in the north were formed (Reijmer et al., 2017), in response to widespread
126 SW-NE directed extension in an extensional collapse setting (Smit et al., 2018), and forming the structural grain
127 of major fault structures in Late Paleozoic and Mesozoic basin history. In the Late Carboniferous increased
128 siliciclastic input from the Variscan thrust front buried the carbonate platforms. Thick shales filled the deep basin
129 north of the orogen, followed by the deposition of fluvio-deltaic sandstones, shales and coals. The collapse of the
130 Variscan orogen led to the formation of the Southern Permian Basin (Doornenbal and Stevenson, 2010; Van

Wees et al., 2000; Ziegler, 1990). Permian deposits, in the Netherlands, are mainly aeolian and fluvial sandstones (Rotliegend Group) overlain by evaporites (Zechstein Group). The evaporites are thick in the north, leading to the occurrence of salt diapirs, walls and domes (Ten Veen et al., 2012). Further south, the salt is absent and the Zechstein deposits are developed in a basin margin facies (Geluk, 2005). The breaking up of Pangea in the Triassic caused subsidence and deposition of shales, followed by fluvial and aeolian sandstones in fault-bounded depocentres (Lower Germanic Trias, De Jager (2007). During the deposition of sediments of the Upper Germanic Trias, subsidence gradually increased, and evaporites (Röt), fluvio-lacustrine and marine marls and limestones of the Muschelkalk were deposited (Geluk et al., 2007). Increased sediment input led to the deposition of lagoonal and evaporite sediments of the Keuper Formation. During the Jurassic, smaller fault bounded basins and highs developed, in the Early Jurassic marine shales were deposited (De Jager, 2007). Rifting in the North Sea leading to doming caused erosion and non-deposition (Wong et al., 2007). In the Late Jurassic and Early Cretaceous, fluvial to shallow marine siliciclastic sediments were deposited in small fault-bound basins (Schieland and Rijnland Groups, De Jager (2007), Willems (2017)). By the end of the Cretaceous, marine shales and carbonates are deposited. In the Late Cretaceous, the northward movement of Africa towards Europe caused the Alpine orogeny, leading to inversion tectonics with uplift and erosion. Increased sediment input led to the deposition of siliciclastic sediments of the Cenozoic North Sea Group. The Quaternary is dominated by fluvio-deltaic, glacial, and coastal depositional siliciclastic sediments. Figure 1 illustrates the tectonic history. It shows areas that, between the Early Carboniferous and Late Jurassic, have remained relatively undisturbed highs in orange, platform areas in green, and inverted basins in blue. The colour coding used in Figure 1 reflects the sedimentary succession that currently exists, and therefore the tectonic history. For instance, in the Friesland Platform area, shown in dark green in the North, Cretaceous sediments are directly overlying Permian Zechstein evaporites, Rotliegendes sandstones and sandstones and shales of the Carboniferous. This is also illustrated in the cross section of Figure 2, which shows the sedimentary units. Note that faults are not shown in Figure 2 because they are not available in the online version of the DGM-deep model, and fault structures were also not incorporated to the thermal model. Also note that the units shown are based on seismic interpretations, and that they do not necessarily correlate fully to the units defined in the ICS timescale.
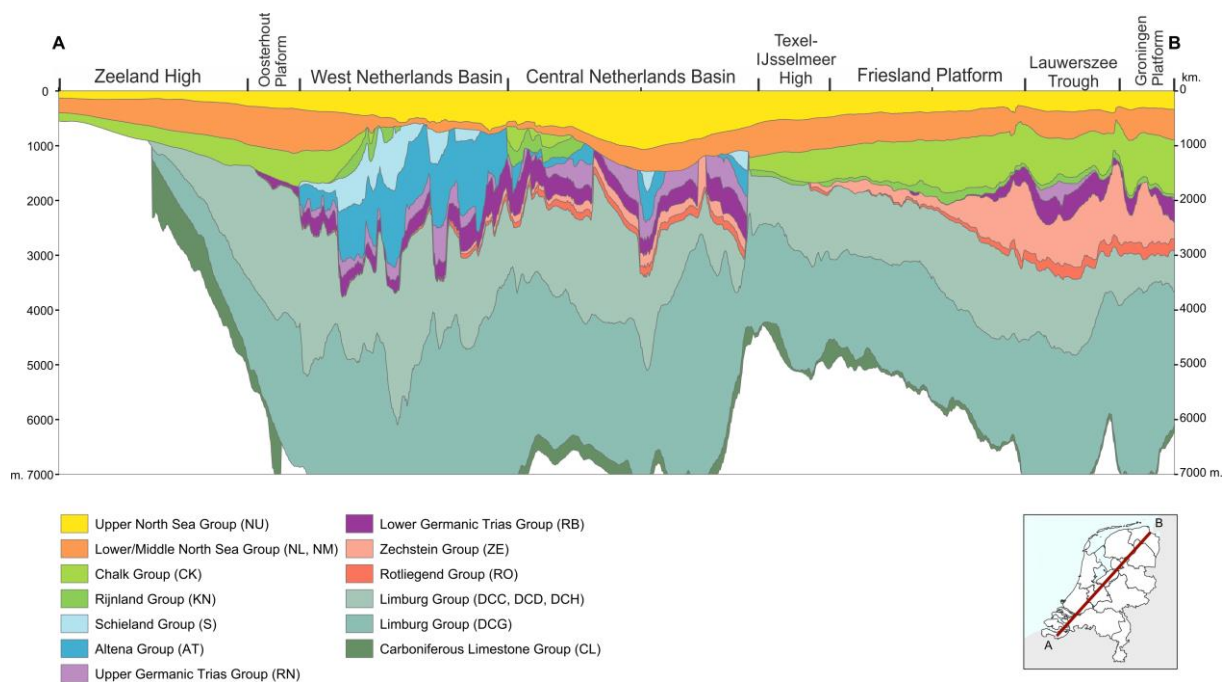
Figure 2. Cross section through the Netherlands showing the the main sedimentary units to the base of the Namurian, adopted from the Netherlands Oil and Gas Portal website (www.nlog.nl). Fault structures are not shown in the section as they were not incorporated to the thermal model.

The tectonic evolution of the Netherlands described above has led to a situation where the reservoirs that have been targeted by the oil and gas exploration for more than 70 years are the same a currently targeted by geothermal exploration now. If earlier unsuccessful attempts like the Asten geothermal well of 1988 are ignored, the exploration for geothermal energy started in the Netherlands around 2006, when the first doublet was drilled.

166 Currently, 25 doublets have been drilled, of which 16 are producing, 4 are suspended, and 5 are not yet
167 producing (source: www.nlog.nl). The energy is used for direct heating purposes, especially greenhouses and in
168 a few cases city heating. This requires temperatures between about 60 and 100 °C. Assuming a geothermal
169 gradient of about 31.3 °C/km and an average surface temperature of 10 °C (Bonté et al., 2012), this temperature
170 range exists approximately between 1.5 and 3.0 kilometers depth. With the exception of two doublets that
171 targeted a fault in Carboniferous limestones, all doublets target sandstone reservoirs having sufficient primary
172 porosity and permeability to produce hot water at such rates that stimulation of the reservoir is not required.
173 Figure 2, a generalized cross section through the Netherlands, shows which reservoirs are found at these depths.
174 The main targets for geothermal exploration are the sandstones from the Rotliegend (mainly in the Northern part
175 of the country), Lower Germanic Trias and Upper Jurassic/Lower Cretaceous (mainly in the West Netherlands
176 Basin). To a lesser extent, fractured Devonian quartzites and Carboniferous Limestones are targeted, and
177 Paleogene sandstones.

178 3.   Subsurface temperature data

179 Subsurface temperature data from the onshore Netherlands are available on the Dutch Oil and Gas portal
180 (http://www.nlog.nl) and on the Dutch Geothermal Platform (https://geothermie.nl). These temperature
181 measurements are based on Bottom Hole Temperature (BHT) data, Drill-Stem Tests (DST) and Repeat
182 Formation Tests (RFT). Although a large number of BHT data are available for the Dutch onshore, correction is
183 required before they can be used for modeling.

184 BHTs are recorded as maximum temperatures from well logs and are assumed to be the highest at the bottom of
185 the drilled well. These temperatures may differ from the actual formation temperatures due to the drilling
186 operations. Corrections of BHT data are most commonly based on analytical methods (e.g. Goutorbe et al.,
187 2007) or statistical methods such as the American Association of Petroleum Geologists (AAPG) correction.
188 Numerous modelling methods are also available (e.g. Luijendijk et al., 2011; Rühaak, 2015) but remain difficult
189 to apply for large datasets.

190 The temperature dataset we used in this study is based on the original database from Bonté et al. (2012),
191 extended with new temperature measurements (Figure 3). For correction of the new BHTs we followed the same
192 workflow as Bonté et al. (2012). The new dataset contains 438 BHTs corrected with the analytical method
193 sampled from 199 wells and 987 statistically corrected BHTs from 401 wells, yielding a total of 1425 BHT
194 temperature values. The total number of raw BHTs is significantly larger than the amount of corrected data, as
195 analytical corrections require multiple measurements (Figure 3c). In addition, the new dataset contains 65 DST
196 and RFT measurements from 36 wells. We also included 17 production temperature measurements from
197 geothermal wells collected from the Dutch Geothermal Platform (https://geothermie.nl).

198 The new database consisting of 1507 temperature measurements from 505 wells (Figure 3a,b). The
199 measurements yield an average geothermal gradient of 31 °C/km. However, there are some deep anomalies with
200 high temperatures such as the LTG-01, TJM-02-S2, and WSK-01 wells (see Figure 9 for locations).
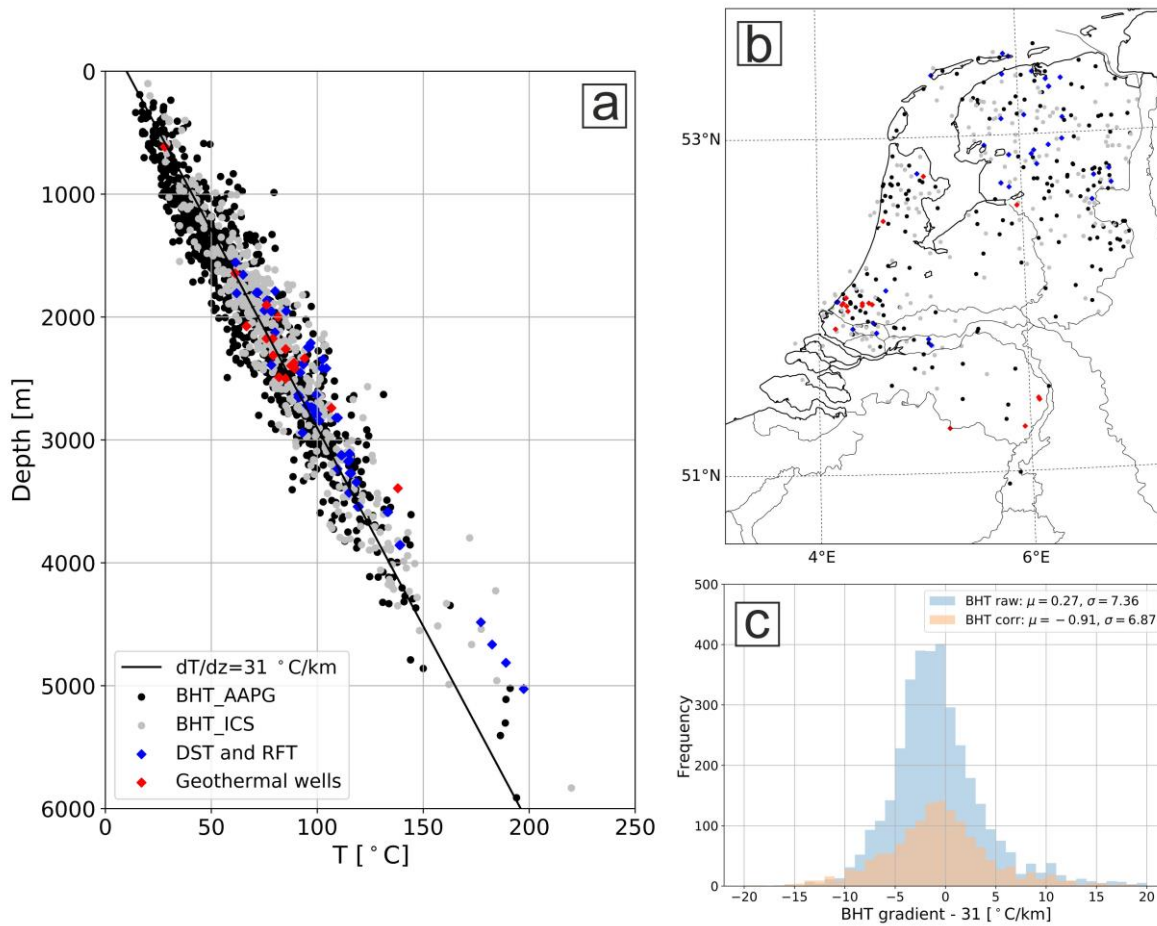
Figure 3. Temperature dataset including BHTs, DSTs, RFTs and production temperatures from geothermal wells modified after Bonté et al. (2012) (a). BHT_ICS: BHTs corrected with analytical method, BHT_AAPG: BHTs corrected with statistical method. The temperature measurements were collected from wells drilled in the onshore Netherlands (b). In case of multiple measurement types in a single well, the one with the lower uncertainty is shown in (b). The misfit of raw and corrected BHT gradients with the average Dutch geotherm are shown in (c), with the mean and standard deviation of the fitted Gaussian functions.

4. Conceptual Model
    4.1. Forward model

The temperature field is forward modeled solving the heat equation in 3D, assuming steady-state conditions and conductive heat transfer only:

$$0 = \nabla \cdot (\lambda \nabla T) + A \qquad [1]$$

where λ is the thermal conductivity, T is the temperature, A is the radiogenic heat generation, and $\nabla = \left(\frac{\partial}{\partial x}, \frac{\partial}{\partial y}, \frac{\partial}{\partial z}\right)$ is the nabla operator. We solve the equation for a low and high resolution hexahedral grid with geometry specifications presented in section 5. Solutions were obtained by a finite-difference approximation using the Preconditioned Conjugate Gradient method (PCG) (Limberger et al., 2018). The boundary conditions at the top were identical for all models: a stationary surface temperature of 8 °C. This value deviates from the average observed yearly surface temperature, which is 10 degrees. We first tested our models with a fixed top boundary condition of 10 °C. Such models systematically overestimated the temperature measurements at depth shallower than 2500 m. To decrease these misfits, we tested our workflow with a lower value of 8 °C, that provided a better fit with the data: the root mean square (RMS) errors at 1000 m and 2000 m (±500 m) depth decreased from 0.8 °C and 0.84 °C to 0.71 °C (Table 3). Therefore, we choose a lower value to our final model to account for the paleo-surface temperatures effected by the recent ice age (e.g. Donders et al., 2009; Verweij et al., 2012). The boundary conditions at the bottom were different for the low- and high-resolution models. We chose a fixed temperature at the bottom of the lithosphere with a corresponding value of 1200 °C for the low-resolution

226 models. The heat flow at 10 km depth, obtained from the low-resolution model, was used as boundary condition
227 for the high-resolution models. The vertical edges of all models were assumed to be insulating with a fixed heat
228 flow of zero.

229 The motivation to use a steady-state model, excluding transient thermal effects, is computational performance
230 for the ES-MDA inversion which requires 100s of model runs. We argue that the use of a steady state model is
231 justified since in most of the Netherlands active tectonic processes are absent or marked by very low
232 sedimentation rates, up to a maximum of 0.1 mm/y in the southeast of the Netherlands, and have resulted in less
233 than 1.5 km of sediments in the last 20 million years. Previously studies, incorporating transient effects,
234 demonstrate that such low sedimentation rates do not deviate considerably from the steady state assumptions
235 (e.g. Van Wees et al., 2009).

236   4.2. Thermal convection in the Dinantian carbonate platforms

237 The previous 3D temperature model from Bonté et al. (2012) could not reproduce the thermal anomaly measured
238 at a depth below 4 km in the LTG-01 well (see Figure 4 for location). Bonté et al. (2012) suggested that higher
239 than expected temperatures and the abnormally low thermal gradient observed within the Dinantian carbonates
240 might be explained by the occurrence of hydrothermal convection. Another possible explanation of the thermal
241 profile observed in the LTG-01 well is the large thermal conductivity contrast between the overlying
242 Westphalian and Namurian layers and the Dinantian carbonates, based on petrophysical analysis in the
243 framework of the SCAN project (Veldkamp and Hegen, 2020). Van Oversteeg et al. (2014) and Lipsey et al.
244 (2016) investigated the potential for thermal convection at the LTG-01 well and confirmed that convection is
245 likely to occur in the Dinantian carbonate platform To come to this conclusion, they assessed the minimum
246 permeability (k_{min}) required for convection based on Rayleigh number analysis following Horton and Rogers Jr
247 (1945) and Lapwood (1948). Lipsey et al. (2016) also supported the occurrence of fluid convection with
248 permeability assessment on core samples and numerical modeling.

249 The Rayleigh number is a dimensionless value that indicates the likelihood of natural or free convection. The
250 equation for the Rayleigh number in a porous medium is written as:

251

$$Ra = \frac{k\rho_f^2 c_p g \alpha_f \Delta TH}{\mu\lambda} \qquad [2]$$

252

253 where k is the permeability, g is the gravitational acceleration, ΔT is the temperature difference between the top
254 and the bottom of the layer, H is the thickness of the layer and ρ_f, c_p, α_f are the density, the specific heat
255 capacity, the thermal expansion coefficient of the pore fluid, respectively. μ and λ denote the viscosity of the
256 fluid and the bulk thermal conductivity of the of the medium. If Ra exceeds a certain threshold value, referred to
257 as the critical Rayleigh number (Ra^*), convection can take place in the medium. For a horizontal, homogenous
258 isotropic porous medium bounded by fixed temperature conditions, $Ra^* = 4\pi^2$. Equation (1) can be rewritten to
259 determine k_{min} using Ra^*:

260

$$k_{min} = \frac{Ra^*\mu\lambda}{\rho_f^2 c_p g \alpha_f \Delta TH} \qquad [3]$$

261

262 The minimum permeability to initiate hydrothermal convection, k_{min} , for the Dinantian carbonates was
263 calculated to be 3x10^{-14} m^2 (Van Oversteeg et al., 2014) and1.9x10^{-14} m^2 (Lipsey et al., 2016). The difference
264 between the two values mostly originates from the different values used for the thickness of the convective layer
265 in the Dinantian carbonates, being 600 m and 800 m, respectively. Since the proposed permeability for the
266 interval of the Dinantian by Van Oversteeg et al. (2014) was estimated to be 6x10^{-14} m^2 and Lipsey et al. (2016)
267 reported the possibility of even higher values (up to 10^{-13} m^2), convection is likely to explain the temperature
268 profile in the LTG-01 well.

269
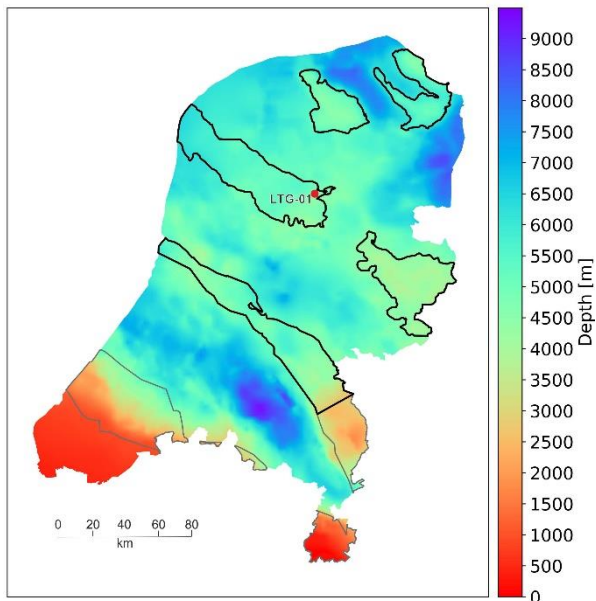
Figure 4. Depth of the top of the Carboniferous Limestone Group (Dinantian). The extent of the carbonate platforms within the group based on seismic data and well logs, adopted from Kalkman (2016), is outlined. We assumed that convection may occur in the deeper platforms, marked by the thick black outline.

Based on these findings, we assumed potential hydrothermal convection in the carbonate platforms all over the Netherlands. However, these carbonate platforms are found at significantly different depths in the Netherlands: in the south the platforms are located much shallower than in the north. (Figure 4). Ra is dependent on the pore fluid properties, which show a significant variation with depth. Van Oversteeg et al. (2014) analyzed the effect of pressure and temperature on k_{min} and showed that k_{min} strongly decreases with depth. We constructed similar k_{min}-depth curves for different layer thicknesses (Figure 5) to assess if convection could occur in the carbonate platforms in the south of the Netherlands. We calculated fluid properties using a model dependent on temperature, pressure, and salinity (after Van Wees et al. (2012)), where the temperature, pressure and salinity dependence of density and viscosity is incorporated after Batzle and Wang (1992), and the temperature and salinity dependence of specific heat capacity is based on Grunnberg (1970). The temperature was calculated with a constant geothermal gradient of 31 °C/km, and the pressure was assumed to be hydrostatic. The minimum Rayleigh permeability at larger depth is relatively small: between 3.5-5.5 km k_{min} ranges from 1 to 5 x 10^{-14} m^2 (Figure 5a). At shallower depth, however, the values are significantly larger (Figure 5b): at 2 km depth and shallower, k_{min} is larger than $\sim 10^{-13}$ m^2, which is equal to the highest permeability of the Dinantian (Lipsey et al., 2016). We thus concluded that thermal convection is not likely to occur in the carbonate platforms in the south.

8
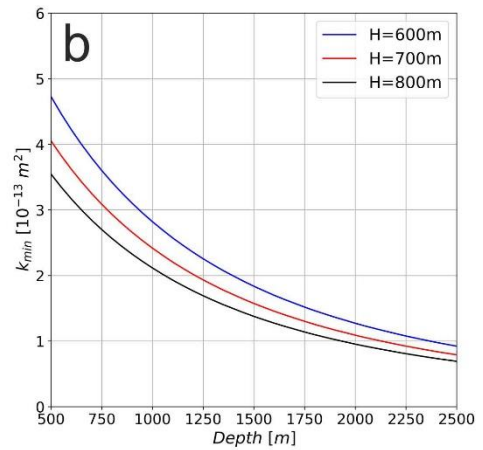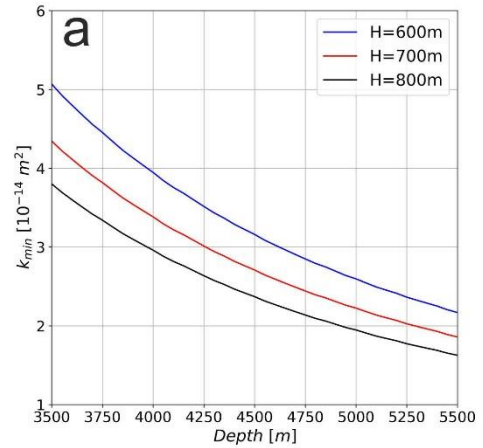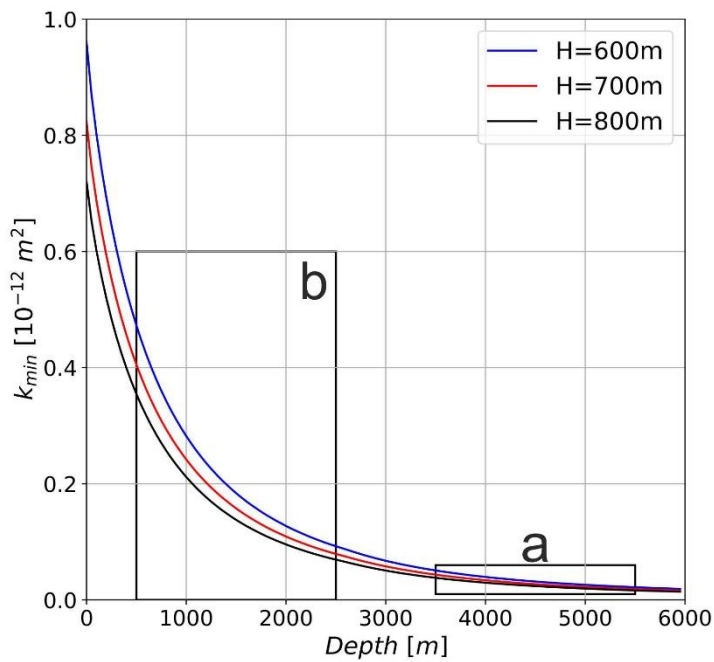
Figure 5. The dependence of minimum Rayleigh permeability on depth. The curves were constructed by taking into consideration the temperature, pressure, and salinity dependency of water properties following Van Wees et al. (2012). Note the different scales for depth and k_{min}.

Our calculations are based on several assumptions: we adopted a horizontal, homogenous isotropic porous medium bounded by fixed temperature conditions. Other factors such as the effect of the extent and geometry of the platform, heterogeneity in permeability can play an important role in the presence/absence of convection (Lipsey et al., 2016). These factors need to be taken into account for site-specific studies. Still, our calculations can be used as an approximation to assess the potential for hydrothermal convection in the Dinantian carbonate platforms all over the Netherlands.

5. Model geometry and thermal properties
5.1. Model geometry

The thermal models have been built in the Dutch coordinate system (EPSG:28992) and their outline has been defined by the political boundaries of the Netherlands. We performed the modelling in two resolutions: the low resolution models extend from the surface up to the depth of the Lithosphere-Asthenosphere Boundary (LAB), while the high resolution models only include the uppermost 10 km of the subsurface. For the low resolution models, temperatures were calculated through a regular 3D grid with a horizontal resolution of 2.5x2.5 km, a vertical resolution of 200 m for the uppermost 10 km, and 3 km down to the LAB. The high resolution models are defined by 1x1 km and 200 m grid spacing in horizontal and vertical directions, respectively.

The model was built as a layered structure that includes the lithospheric mantle, lower crust, upper crust and 14 sedimentary units, summarized in Table 1. For the thickness of the lithosphere we used a constant value of 110 km. We also tested models for the LAB depth after Tesauro et al. (2009) and Artemieva (2019), but the thermal effect of the different LAB models in the shallow part of the model (0-10 km) was negligible. The crustal thickness was adopted from the EuCRUST-07 model (Tesauro et al., 2008) with an average thickness of 32 km

313 in the Netherlands. For the subdivision of the sedimentary layers we followed the DGM-deep v4.0 onshore
314 model (adopted from nlog.nl, Figure 2). The sedimentary model is available to the base of the Limburg Group,
315 since the depth of the base of the Carboniferous Limestone Group (Dinantian) is not yet well constrained in all
316 parts of the Netherlands. We estimated the thickness of the Dinantian to be 700 m, which is a rough average of
317 the thicknesses found in the LTG-01 and UHM-02 wells that drilled the entire Dinantian section. It is important
318 to note that the thickness of the Dinantian might be lower in some areas. For example, in the southern part of the
319 Netherlands, where the Dinantian is shallower, the estimated thickness is mostly below 500 m (Reijmer et al.,
320 2017). We selected a constant thickness of 700 m based on the assumption that older sediments with similar
321 thermal properties are likely to be present below the Dinantian.

322 Following the example of the thermal anomaly found in the Dinantian carbonates in the Luttelgeest-01 (LTG-01)
323 well, we assumed that hydrothermal convection may occur in the carbonate platforms. To distinguish between
324 the basin facies and platform areas of the Dinantian, we treated the carbonate platforms as a separate layer by
325 adopting their geometry after Kalkman (2016) (Figure 6), based on 2D and 3D seismic data and 15 well logs.
326 The outline of the platforms is marked by larger uncertainty in the northern part of the country, where the
327 platforms are deeply buried (Figure 4). Also, in the South there are multiple wells drilling the Dinantian
328 carbonates, providing constraints for the seismic data. We excluded the platforms in the South from the new
329 layer, assuming that hydrothermal convection is most likely restricted to larger depths.

330 In the southern part of the Netherlands we included a new layer to represent the deeply buried Palaeozoic
331 sediments with low porosity below the Dinantian (Figure 10, layer 12). We constructed this layer based on cross-
332 sections from Duin et al. (2006), although its geometry is poorly constrained due to the lack of available data.
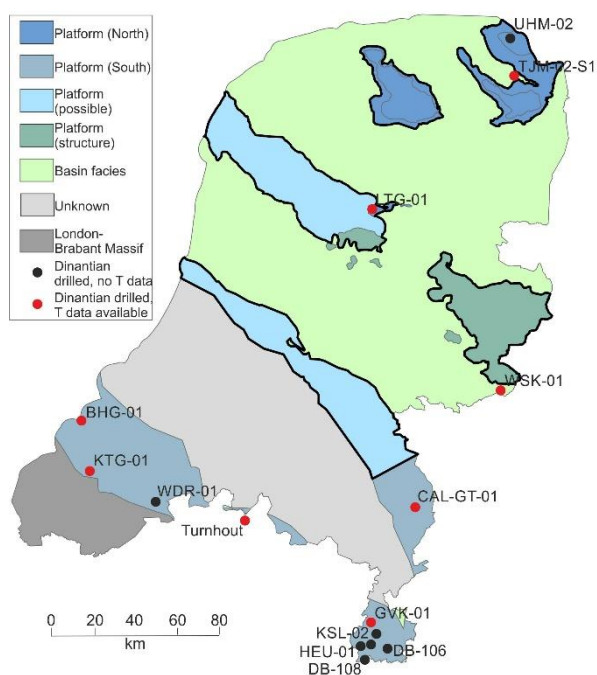
333

334 *Figure 6. Map showing the locations of the Dinantian carbonate platforms and other rocks of Dinantian age*
335 *modified after Kalkman (2016). We use scaling of the thermal conductivity to approximate the thermal effects of*
336 *convection. Outlined in black are the areas below the carbonate platforms for which we scaled the thermal*
337 *conductivity values.*

338   5.2. Thermal properties
339   5.2.1. Thermal conductivity

340 We defined the thermal properties of each sedimentary unit based on their lithologies following the methodology
341 of Hantschel and Kauerauf (2009) (Table 1). The bulk matrix thermal conductivity (λ_m) of the lithological
342 components were corrected for pressure conditions and the in-situ temperature after Sekiguchi (1984). For shales
343 and carbonates, we took into consideration the change in anisotropy with increasing compaction (Hantschel and
344 Kauerauf, 2009). The horizontal matrix conductivity was calculated from λ_m using the anisotropy factors of the

10

345 corresponding lithology. We obtained the bulk thermal conductivity (λ_{bulk}) for each lithology by taking the
346 geometric mean of k_m and the temperature-dependent thermal conductivity of the pore fluid (λ_w) as follows:

347

$$\lambda_{bulk}(z) = \lambda_m^{1-\phi} * \lambda_w^{\phi} \qquad [4]$$

348

349 where ϕ is the porosity. If a sedimentary unit consisted of different lithologies, the bulk thermal conductivity
350 within the layer was calculated by taking the harmonic mean of the bulk conductivities.

351 Because our forward thermal model only solves the steady-state heat equation for conduction, we used a pseudo-
352 convective approach to reproduce the deep thermal anomaly found in the LTG-01 well: we scaled the prior
353 thermal conductivity of the layer corresponding to the carbonate platforms. This method, together with a similar
354 modelling technique, was applied by Békési et al. (2017) for the Pannonian basin. After several model runs to
355 test different thermal conductivity values of the platform layer, we could not reproduce the deep thermal
356 anomaly. Our models managed to fit the convective profile only by the combination of increasing the thermal
357 conductivity of the platforms and decreasing the conductivity of the layer overlain by the Dinantian (Limburg
358 Group). We tried to choose the thermal conductivity of the layer corresponding to the Limburg Group close to its
359 original value, but low enough to fit the temperature measurements in the Dinantian. We tested numerous
360 combinations before attaining acceptable values. We fixed the thermal conductivity of the Limburg Group to 1.5
361 W m^{-1} K^{-1}, and the Dinantian carbonate platforms to 5.0 W m^{-1} K^{-1} (Table 1). It is important to note that scaling
362 the thermal conductivities of limestones to unrealistic values of 5 W m^{-1} K^{-1} was required to approximate the
363 effect of convection with a purely conductive model. The low thermal conductivity of 1.5 W m^{-1} K^{-1} assigned to
364 the Limburg Group is also rather unrealistic, considering its compaction and low porosity. However, Silesian
365 sediment with high coal content might explain such low values. We used these values as prior thermal
366 conductivities before applying the data assimilation.

367 The thermal conductivity of the upper and lower crust were estimated with the temperature- and pressure-
368 dependent relation of Chapman (1986). With increasing temperature down to the lithospheric mantle, the
369 contribution of the radiative component of the thermal conductivity increases compared to the contribution of the
370 lattice component. Therefore, the thermal conductivity of the lithospheric mantle was calculated as the sum of
371 the temperature-dependent radiative contribution obtained after Schatz and Simmons (1972) and the
372 temperature- and pressure-dependent lattice component following the formula of Xu et al. (2004). More details
373 on the calculations of the thermal conductivity values of the different units are described by Limberger et al.
374 (2018).

375   5.2.2. Radiogenic heat production

376 For the radiogenic heat production of each sedimentary unit, a constant value was selected based on generic
377 values of typical lithologies from Hantschel and Kauerauf (2009). The heat production of the layers consisting of
378 more than one lithology was calculated as the geometric mean of the corresponding lithologies. We chose 1 μW
379 m^{-3} as a prior value for heat generation in the upper crust, which was then updated through data assimilation to
380 account for potential under/overestimation of the initial radiogenic heat production. For heat generation in the
381 lower crust and lithospheric mantle, we assigned 0.5 and 0.02 μW m^{-3}, respectively, also following Hantschel
382 and Kauerauf (2009).

383

ID	Layer name	Age of sedimentary units	Lithology	Thermal conductivity [W m^{-1} K^{-1}]	Anisotropy factor	Radiogenic heat generation [μW m^{-3}]
1	Upper North Sea Group	Neogene and Quaternary	50 % Shale - 50 % Sandstone	Pressure- and temperature-dependent based on lithotypes after Hantschel and Kauerauf (2009)	Constant values of each lithotype after Hantschel and Kauerauf (2009), used to calculate the horizontal matrix conductivity of the different lithotypes. For shales and carbonates, we took into consideration the change in anisotropy with increasing compaction (Hantschel and Kauerauf, 2009)	Constant values per layer based on lithotypes after Hantschel and Kauerauf (2009). The heat production of the layers consisting of more than one lithology was calculated as the geometric mean of the corresponding lithologies.
2	Lower and Middle North Sea Group	Paleogene	50 % Shale - 50 % Sandstone			
3	Chalk Group	Upper Cretaceous	100 % Chalk			
4	Rijnland Group	Lower Cretaceous	50 % Shale - 25 % Marl - 25 % Sandstone			
5	Upper Jurassic Groups	Upper Jurassic	50 % Shale - 50 % Sandstone			
6	Altena Group	Lower and Middle Jurassic	75 % Shale - 25 % Silt			
7	Lower and Upper Germanic Groups	Triassic	40 % Shale - 30 % Limestone - 30 % Sandstone			
8	Zechstein Group	Lopingian (Late Permian)	Zechstein layer (Shale to the South - Salt to the North)			
9	Upper Rotliegend Group	Late Guadalupian (Middle Permian)	70 % Sandstone - 15 % Shale - 15 % Silt			
10	Caumer Subgroup	Westphalian (Carboniferous, Middle Silesian)	60 % Shale - 40 % Sandstone			
11	Limburg Group	Namurian (Carboniferous, Lower Silesian)	60 % Shale - 40 % Sandstone	1.5		
12	Carboniferous Limestone Group – carbonate platforms	Dinantian (Lower Carboniferous)	100 % Limestone	5		
13	Carboniferous Limestone Group	Dinantian (Lower Carboniferous)	100 % Limestone	Pressure- and temperature-dependent based on lithotypes after Hantschel and Kauerauf (2009)		
14	Old Paleozoic sediments	Paleozoic (Devonian and older)	60 % Shale - 40 % Sandstone			
-1	Upper crust	-	100 % Granite	Pressure- and temperature-dependent after Chapman (1986)	-	1
-2	Lower crust	-	100 % Anorthosite		-	0.5
-3	Lithospheric mantle	-	100 % Peridotite	Pressure- and temperature-dependent after Schatz	-	0.02

|				and Simmons (1972) and Xu et al. (2004)		

384   *Table 1. Lithological composition and prior thermal properties of the layers.*

385

386 6. Modeling work flow
387   6.1. Description of the work flow

388 To construct the thermal model of the deep subsurface of the Netherlands, we first adopted the prior thermal
389 properties of the layers listed in Table 1. Initial calculations were made by solving the heat equation in multi-1D
390 (step 1, Figure 7) in the low resolution grid, in order to obtain default values for thermal conductivity in
391 agreement with first order estimates for temperature and pressure. Subsequently, based on these default
392 properties we calculated a prior 3D thermal model (step 2 Figure 7).

393 The misfit between modeled and observed temperatures was subsequently reduced by updating the thermal
394 properties of the layers using ES-MDA in step 3-4 (Figure 6). The results are subsequently used in a higher
395 resolution grid and the final posterior thermal model is obtained in step 7, as shown in Figure 7 and described in
396 the following sections.
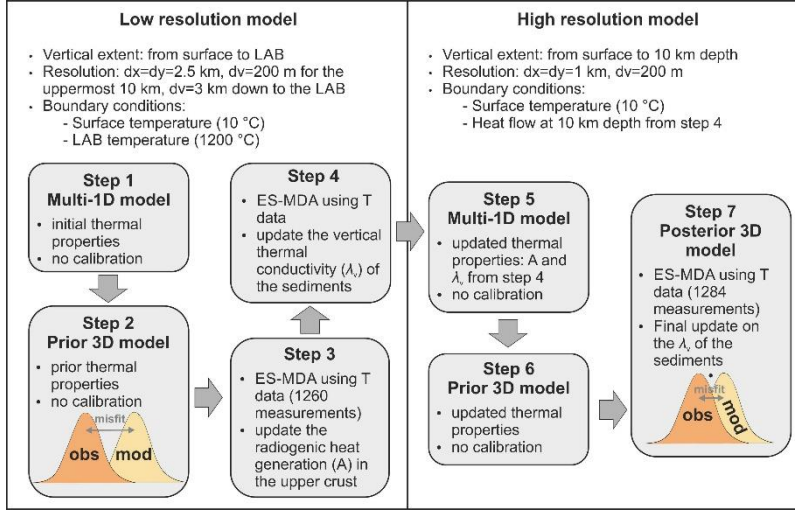
397

398 *Figure 7. Description of the modeling work flow.*

399 7. Inversion

400 We used inversion of subsurface temperature data to infer the thermal field by varying a selection of the thermal
401 properties of the layers: the radiogenic heat generation of the upper crust and the thermal conductivity of the
402 sedimentary units.

403   7.1. Ensemble Smoother with Multiple Data Assimilation (ES-MDA)

404 We solved the inverse problem using the Ensemble Smoother (ES), which estimates the parameters in a single
405 step by a global update incorporating all data available (Emerick and Reynolds, 2013a). Ensemble-based
406 methods, such as the Ensemble-Kalman Filter (EnKF) and the ES, are suitable for systems with large numbers of
407 parameters. Emerick and Reynolds (2013b) investigated different ensemble methods and found that in case of
408 non-linear forward models, the Ensemble Smoother with multiple data assimilation (ES-MDA) performs better
409 than the EnKF. Additionally, the ES-MDA is computationally less demanding. Therefore, we applied the ES-
410 MDA for handling the non-linearity between the observations and model parameters.

411 For the ES, the assimilated model parameter vectors m^a are written as (Emerick and Reynolds, 2013a):

$$m_j^a = m_j^f + C_{MD}^f \left(C_{DD}^f + C_D \right)^{-1} \left(d_{uc,j} - d_j^f \right) \qquad [5]$$

412 for *j = 1, 2, [...], N$_e$*, where N_e denotes the number of ensembles, C_{MD}^f is the cross-covariance matrix between the
413 prior vector of model parameters, m^f, and the vector of predicted data, d^f. C_{DD}^f is the $N_d \times N_d$ auto-covariance
414 matrix of predicted data, and C_D is the $N_d \times N_d$ covariance matrix of the measurement errors, where N_d denotes
415 the number of measurements assimilated. $d_{uc} \sim N(d_{obs}, C_d)$ is an ensemble of vectors with the measurements
416 vector d_{obs}, perturbed normally according to the covariance matrix C_d. An ensemble of solutions is produced by
417 the ensemble update, consistent with the prior statistics, and the mean of the ensemble is taken as the best
418 estimate. In case of the ES-MDA, an ES is applied multiple times, with the output ensemble used as input for the
419 next update. The number of data assimilation steps or iterations, N$_a$ must be selected a-priori. The data

420 covariances used for the update steps are increased by a multiplication factor, α_i for $i=1,2..., N_a$, and α_i must be
421 selected as $\sum_{i=1}^{N_a} \frac{1}{\alpha_i} = 1$. This covariance adjustment to increase ensemble variance is required to reduce filter
422 divergence and to improve performance of the state vector.

423 ### 7.2. Data uncertainty

424 We used the temperature measurements as observations for the inversion. We assigned uncertainties to the
425 temperature data based on measurement quality and assuming a Gaussian error distribution. We made this
426 assumption after assessing the misfits of the raw and corrected BHT gradients with the average geothermal
427 gradient, that can be approximated with normal distribution (Figure 3c). It is important to note that measurement
428 errors are not necessarily symmetric and they are depth-dependent (e.g. Agemar et al., 2012). Here we select
429 identical uncertainties for the same measurement types with the same correction method for simplicity.
430 Uncertainties may be overestimated due to the fact that we choose maximum values assigned to each category.
431 We marked the DSTs and RFTs with an uncertainty of ±8 °C (e.g. Bonté et al., 2012). For the BHTs, we chose
432 different uncertainties based on the correction method applied to the measurement. We used ±10 °C for BHTs
433 corrected with the analytical method and ±15 °C for values obtained by the statistical method (Goutorbe et al.,
434 2007). The production temperatures of the geothermal wells were treated with an uncertainty of 5 °C. Saeid et al.
435 (2013) suggested that the maximum drop in in production temperatures occur within the first years of operation.
436 Additionally, temperatures of the extracted fluids decrease before reaching the wellhead. Since ~half of the
437 production temperatures were obtained within the first year of production (geothermie.nl), we concluded that the
438 uncertainty of ±5 degrees is a good approximation.

439 During the inversion, only one observation within a grid cell is used. When multiple measurements were present,
440 inversion was limited to the measurement with the lowest uncertainty. As a result, the number of observations in
441 the high-resolution model (1284) was larger than for the low-resolution models (1260, Figure 7). Most of the
442 temperature measurements (~85 %) were conducted at depths below 3 km, ensuring a good calibration for the
443 upper part of the model. At larger depths, the amount of controlling points significantly decreases (Figure 3,
444 Table 3.).

445 ### 7.3. Description of the data assimilation procedure

446 Through the data assimilation, the prior thermal properties including the heat production in the upper crust and
447 thermal conductivity of the sediments were updated to achieve a better fit with the temperature observations. The
448 prior uncertainty in the thermal properties was taken into account by scaling the parameters to a triangular
449 distribution. The spatial variability of the parameters was determined through a spherical variogram. The radius
450 of the variogram is expressed in cells, which corresponds to a certain distance in kilometers.

451 We obtained the posterior thermal model in 7 steps (Figure 7), where steps 3, 4 and 7 included the parameter
452 updates summarized in Table 2. In each step the ES-MDA was run with 600 ensembles and 4 iterations. We
453 chose 4 iterations following the example of Emerick and Reynolds (2013b). In step 3, we scaled the upper
454 crustal heat generation between 0.6 and 1.6 of the prior value, with a variogram range of 14 cells (corresponding
455 to ~42 km). Then, the thermal conductivity of the sediments was scaled between 0.7 and 1.3, except for the
456 Zechstein Group (layer 8) and the Carboniferous Limestone Group (layers 12 and 13), where a larger variation
457 was allowed. We chose scaling factors of 0.7 and 1.4 for the Zechstein Group (layer 8) to account for potential
458 higher thermal conductivity of salts. We scaled the thermal conductivity of the Carboniferous Limestone Group
459 (layers 12 and 13) using a larger range, to allow for more variance approximating the thermal effect of
460 hydrothermal convection (especially in the platform areas). We assumed a smaller-scale lateral variation in the
461 thermal conductivity of the sediments (layer 1-11, 13): in step 4, the range of variations was set to 8 cells (~24
462 km). In the last modelling step (step 7), further refinement of the thermal conductivity of the sediments was
463 achieved by scaling the values between 0.8 and 1.2 with a variogram range of 30 cells (~30 km).

464

465

Modeling step	Description	Prior distribution	Scaling parameters	Variogram model	Variogram range	Number of ensemble runs and iterations
3	update the heat production (A) in the upper crust	Triangular	A: 0.6 and 1.6 for layer -1	Spherical	14 cells (~42 km)	600 ensembles, 4 iterations
4	update the vertical thermal conductivity (λ_V) in the sediments		λ_V: 0.7 – 1.3 for layer 1-7, 9-10, 14 λ_V: 0.7 – 1.4 for layer 8 λ_V: 0.6 – 1.4 for layer 12-13		8 cells (~24 km)	600 ensembles, 4 iterations
7	update (refine) λ_V in the sediments		λ_V : 0.8 – 1.2 for layer 1-13		30 cells (~30 km)	600 ensembles, 4 iterations

466   *Table 2. Overview of the data assimilation procedure.*

467   8.   Results

468   We show the results of the 7-step modeling workflow, yielding the posterior 3D temperature model of the
469   onshore Netherlands in Figure 8. Temperature slices of 1-6 km depth are presented in 1 km intervals (Figure 8).
470   Modeled temperatures at 1 and 2 km depth show a similar pattern: the hottest area is located in the north,
471   corresponding to the youngest sedimentary units of Neogene to Upper Cretaceous age (Upper North Sea Group,
472   Lower and Middle Sea Group and Chalk Group). At larger depths, the most significant positive anomaly is
473   observed near the location of the LTG-01 well. At 3 km depth, the highest temperatures are modeled near the
474   Belgian border in the south, where Dinantian carbonate platforms are located at relatively shallow depth. Higher
475   temperatures at 4 km depth correlate with the extent of the Dinantian carbonate platforms. This correlation is
476   also observed in the 5 and 6 km depth slices, although the anomalies are more pronounced towards the north and
477   near the LTG-01 well. The Zeeland High and Limburg High appear to be relatively cold at larger depth.

478

479
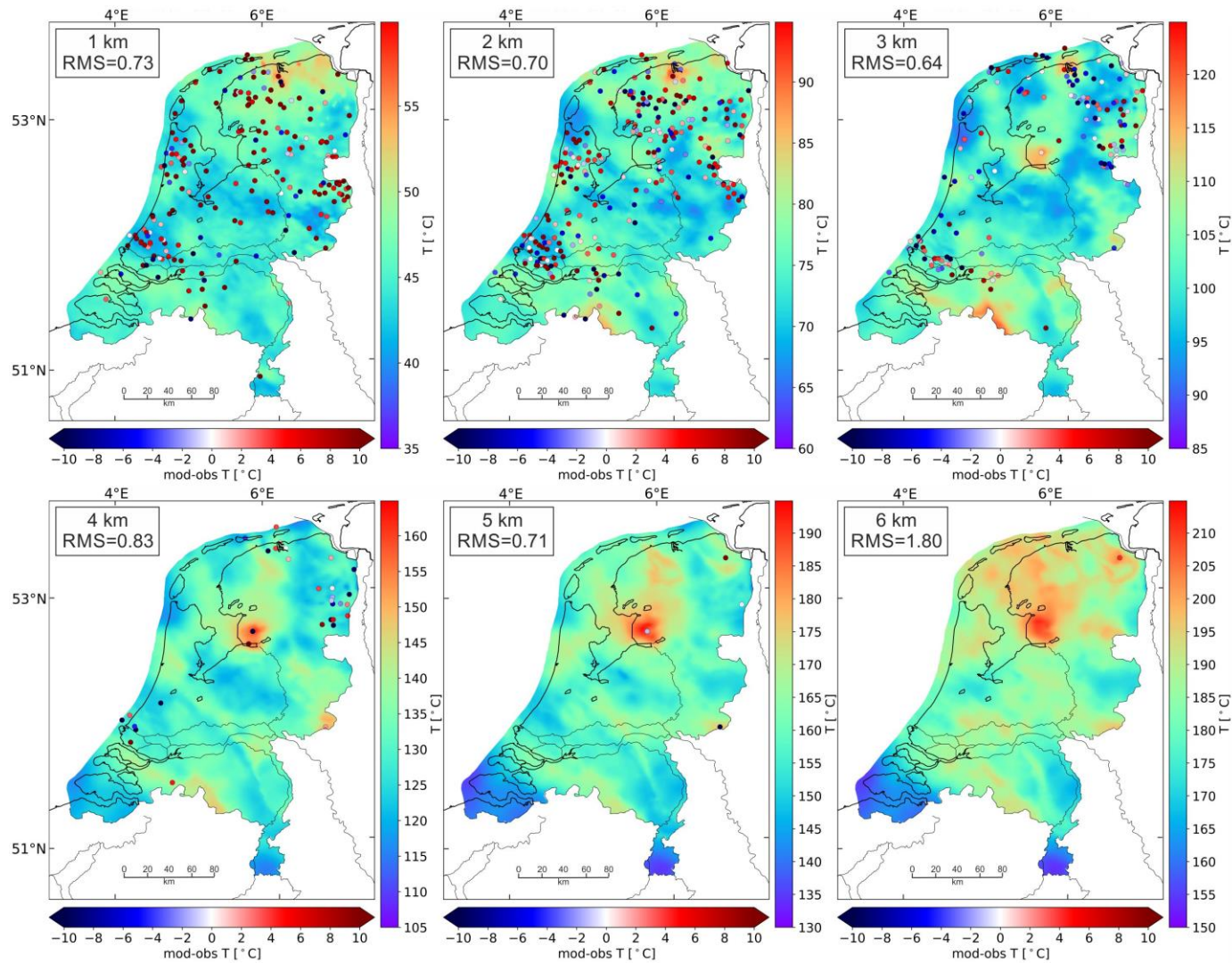
Figure 8. Temperature maps of the final posterior model (step 7 in Figure 7) at 1-6 km depth. The misfits between modeled temperature and measurements (modeled-observed values) within a ±200 m interval are plotted with circles. 80% of the misfits lie within the ±10 °C interval, where the remaining 20% are dominantly attributed to measurements with the largest uncertainty (±15 °C, BHTs corrected with statistical method). Note the different color scale for the modeled temperatures at various depth.

483   To compare our models with the temperature measurements, we constructed 1D profiles at several well locations
484   (Figure 9). We show both the prior and the posterior model results to demonstrate the model improvements after
485   calibration. As prior model we use the uncalibrated model from step 2 in Figure 4.

486   Prior and posterior model temperatures are almost identical at the locations of the KTG-01, LUT-06, HLH-GT-
487   01,and WWK-01 wells, showing a good fit with the measured temperatures (Figure 9). The thermal conductivity
488   profiles show little variation, suggesting calibration was not necessary to improve the fit. For the remaining
489   profiles, the thermal conductivity of the layers was varied resulting in a better fit of the posterior model with the
490   measurements. For instance, the prior model overestimates temperatures at the location of the MKP-14 well.
491   Decreasing the thermal conductivity of the Rijnland Group (layer 4) and increasing the thermal conductivity of
492   the Altena Group (layer 6), resulted in a reduced average geothermal gradient, in good agreement with the
493   measurements. In the LTG-01 and WSK-01 wells, the prior model underestimates the temperatures especially
494   below 3 km depth. To fit the high temperatures in the LTG-01 well, an even lower thermal conductivity was
495   required for the Caumer Subgroup (layer 10) and Limburg group (layer 11) to increase the geothermal gradient
496   above the Dinantian carbonate platform (layer 12). Even though the misfit of our prior model with the WSK-01
497   well measurement is low, a small reduction (~0.2 W m^{-1} K^{-1}) of the conductivity for layer 11 was still necessary
498   to reproduce the measured values.
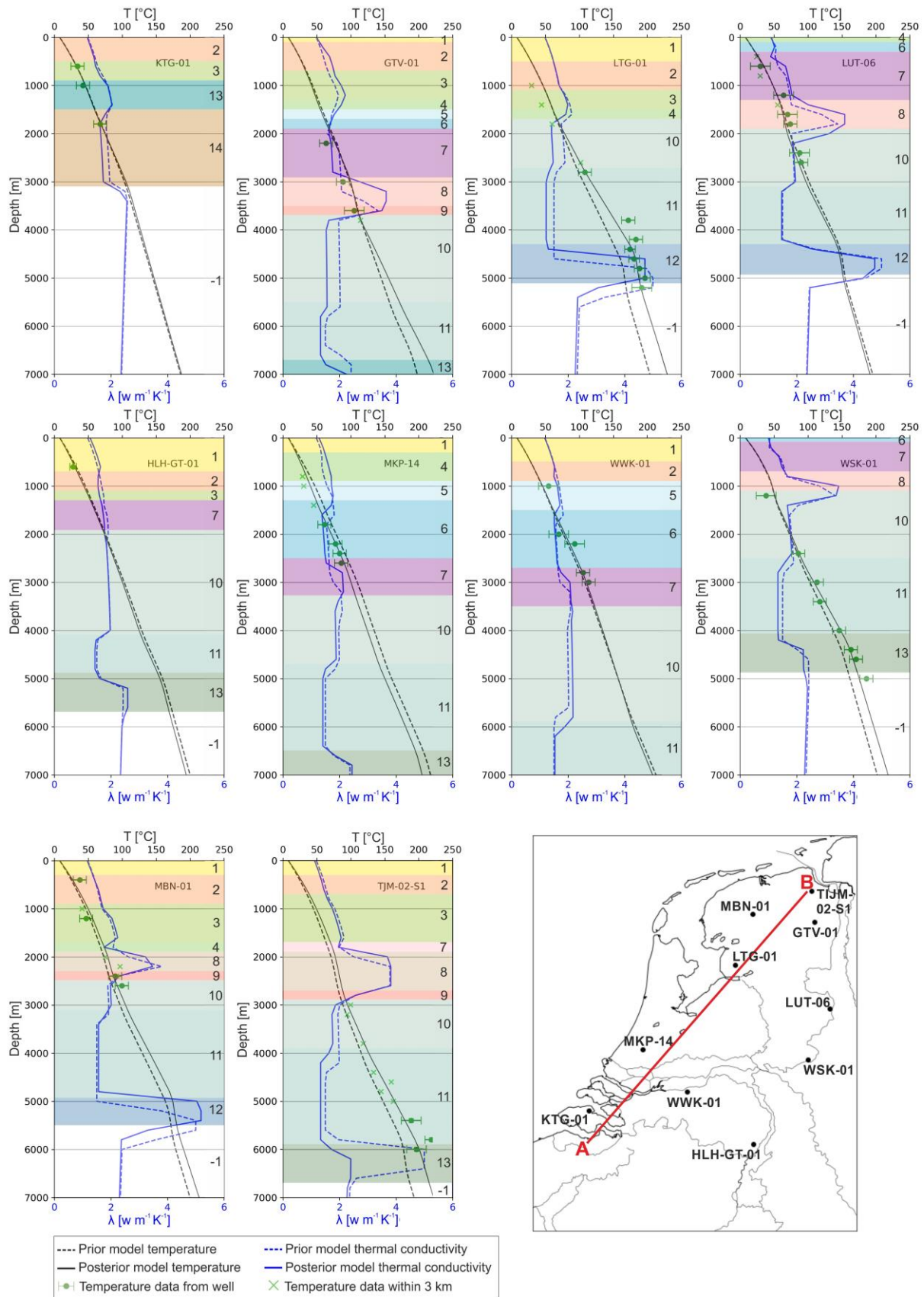
Figure 9. Temperature-depth (black) and thermal conductivity-depth (blue) profiles of the prior model (dashed lines) and posterior model (solid lines) at different well locations. The temperature measurements from the wells are marked by green dots with corresponding error bars. Measurements from wells within 3 km distance are plotted with green crosses. The numbering of the layers corresponds to Table 1. Note that the depth ranges of

Posterior model temperatures are presented along a section crossing the onshore part of the Netherlands from SW to NE (Figure 10). Temperatures up to 1 km depth show slight variations corresponding to changes in the lithology of the layers. At larger depths, more fluctuations are observed within the sediments. For instance, in the NE, where the thickness of the Zechstein Group (layer 8) is the largest, temperatures are higher above and lower below the salt layer. The geothermal gradient in the top 3 km corresponds to ~30 °C/km. The insulating effect of the sediments is observed at larger depth: temperatures are lower within the basement and higher in the basins in the SW at 3-7 km depth. The heat chimney effect of the Dinantian carbonate platforms (layer 12) approximated by increasing thermal conductivity, results in generally higher temperatures above, and lower temperatures below the layer. The hottest area along the section below 3 km depth corresponds to the location of the LTG-01 well, where temperature measurements suggest the presence of hydrothermal convection. The geothermal gradient varies significantly with larger depth: it is generally lower in the basement and in the highly conductive carbonate platforms, and higher in the sediments with a lower conductivity, especially in the layers overlaying the platforms.
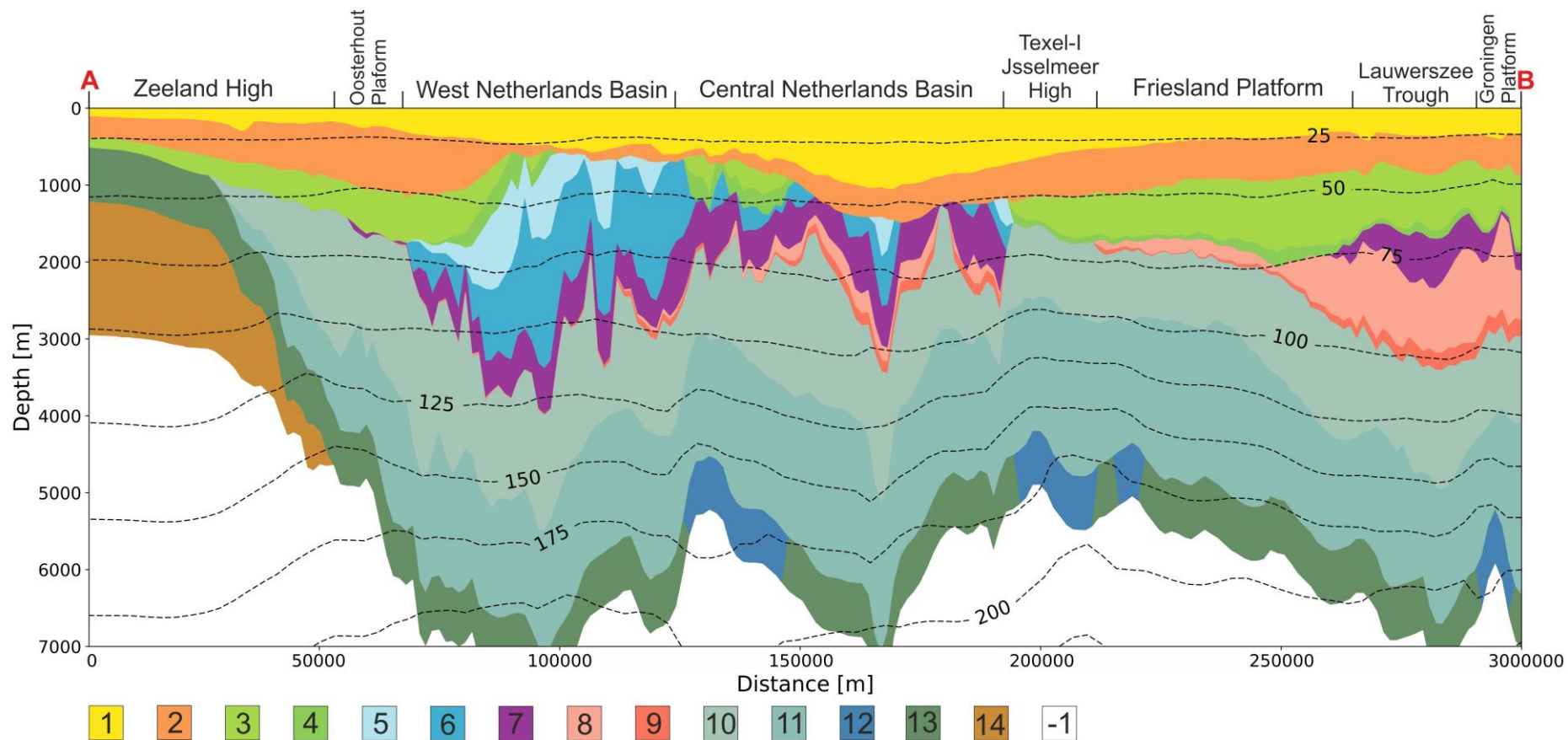
Figure 10. NW-SE cross-section through the onshore Netherlands showing the geometry of the sedimentary units and the depth of the top of the basement (white) used for the modeling. Superimposed are the isotherms from the posterior temperature model. The trace of the cross-section is shown in Figure 9. Layer numbering corresponds to Table 1. The extent of the main Jurassic and Early Cretaceous basins, highs, and platforms along the section is adopted from Kombrink et al. (2012). Fault structures are not shown in the section as they were not incorporated to the thermal model.

After ES-MDA calibration the posterior model shows an improved fit with the measurements compared to the prior model: temperature observations are closer to the P50 results of the posterior model (Figure 11). On the other hand, some of the data points fall outside the bandwidth of the variation of the ensembles. It suggests that the ensemble variance generated with the data assimilation procedure was not entirely sufficient to reproduce the observed variation within the data, especially at shallow depth.

The mean, median, and RMS misfits normalized to data error of the prior and posterior model are summarized in Table 3. After ES-MDA calibration, overall RMS, including all the measurements, decreases from a value of 0.95 for the prior model to 0.70 for the posterior model. Analyses of the misfits at different depth intervals suggest that the prior model overestimates temperatures at shallower depth (1-2 km), but underestimates temperatures at larger depth. The posterior model shows the same trend, but with lower misfits, especially below 3 km depth. The total mean and median of the prior model are smaller than the corresponding values of the posterior model. This is due to the fact that the positive and negative misfits at different depth cancel out, and it is not representative in terms of the goodness of the fit.
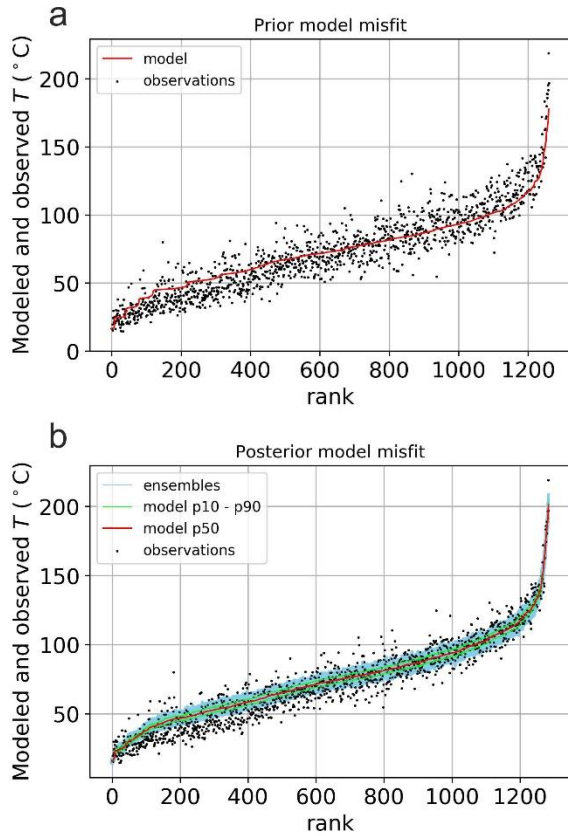
Figure 11. Distribution of the modeled and observed temperatures ranked by the modeled temperatures at the observation points for the prior (a) and posterior (b) models. Temperature measurements are marked by black dots. The red curves indicate the model results (in (b) the P50 values), the green lines in (b) are the P10 and P90 values. The blue interval in (b) indicates the modeled temperatures for all the 600 ensemble members of the last iteration.

Depth [m]	Number of observations for prior model	Number of observations for posterior model	Type of misfit	Prior model misfit	Posterior model misfit
1000 ± 500	368	377	Mean	5.88	4.85
			Median	7.16	6.03
			RMS	0.80	0.71
2000 ± 500	474	487	Mean	2.04	2.03
			Median	2.31	2.32
			RMS	0.86	0.71

3000 ± 500	286	288	Mean	-4.84	-1.44
			Median	-4.39	-1.21
			RMS	1.03	0.67
4000 ± 500	77	77	Mean	-10.25	-1.83
			Median	-9.65	-1.92
			RMS	1.49	0.76
5000 ± 500	12	12	Mean	-19.66	-3.21
			Median	-21.39	-3.91
			RMS	2.21	0.70
6000 ± 500	2	2	Mean	-32.01	-10.12
			Median	-32.01	-10.12
			RMS	3.41	1.80
Total (0-6000)	1260	1284	Mean	0.48	1.67
			Median	1.68	1.97
			RMS	0.95	0.70

Table 3. Mean, median, and RMS misfits in °C of the prior and posterior models normalized to data error. The misfits are reported at 1-6 km depth, including measurements within a ±500 m interval. The overall misfits are calculated using all the measurements.

9. Discussion

We constructed 3D physics-based temperature models for the onshore Netherlands calibrated with 1507 temperature measurements. We performed the modeling in seven steps, starting from lithospheric-scale models with two different resolution steps in vertical direction. The advantage of such large-scale temperature models is that they are able to account for the thermo-mechanical state of the whole lithosphere, which has major influence on temperatures at depths relevant for geothermal exploration (Cloetingh et al., 2010). The boundary conditions of the high-resolution models, extending from the surface to 10 km depth, were derived from these low-resolution lithospheric-scale models. We incorporated temperature measurements for subsequent model steps through an inversion procedure using ES-MDA. Misfits between modeled and observed temperatures decreased during the data assimilation by varying the thermal properties of the sedimentary units and the upper crust. To account for uncertainties of the thermal conductivity in different sedimentary units and the radiogenic heat generation in the upper crust, we scaled the values to triangular distributions. Scaling parameters were determined according to the uncertainties we assigned to each layer. The spatial variation in the properties was introduced through variograms. We selected the size of the variograms based on the wavelengths of perturbations we expected for the thermal properties.

One of the main aspects of our study was to account for the thermal anomaly found in the LTG-01 well. Bonté et al. (2012) suggested that the high temperatures that were measured could be explained by the presence of a magmatic intrusion with high radiogenic heat production formed during the Variscan orogeny (Ziegler, 1990). As an alternative, they proposed the occurrence of hydrothermal convection in the Dinantian carbonate platform situated at depths below 4 km. Based on fracture permeability assessments and numerical modeling, Van Oversteeg et al. (2014) and Lipsey et al. (2016) concluded that convection is likely to occur in the carbonate platforms at the location of the LTG-01 well. The thermal state of the deep subsurface is important for geothermal exploration that targets the deeply buried Devonian-Carboniferous carbonate formations in the Netherlands. These reservoirs are potentially suitable for industrial heating applications and electricity production. To this end, our goal was to identify possible locations where convection in these carbonate platforms might occur and that currently lack temperature measurements.

We assessed the minimum permeability required for convection in different depth intervals based on Rayleigh-number analysis. Given the permeabilities derived from petrophysical data on the Dinantian carbonates, we found that the occurrence of convection is unlikely in carbonate platforms at depths shallower that 2 km. Locally, karstification or faults and fractures might still lead to sufficient secondary permeability allowing for hydrothermal convection. However, this is currently not supported by observations. We assumed that convection might only occur in Dinantian carbonate platforms below 2 km depth, having sufficient permeabilities due to karstification. We assumed that the carbonate platforms in the Dutch subsurface have similar properties. However, the tectonic setting, sea level and burial/diagenesis history vary for the areas, resulting in different platform geometries and reservoir properties (Lipsey et al., 2016).

585 Since our forward model is purely conductive, we approximated the thermal effect of hydrothermal convection
586 by varying the thermal conductivity of the platforms and the overlying layers. We applied this method based on
587 the fact that long term thermal effects can be approximated by a pseudo-convective approach, where the
588 convective layer is marked by a higher than natural thermal conductivity (e.g. Beglinger et al., 2012; Luijendijk
589 et al., 2011; Schmeling and Marquart, 2014). A similar approach was applied by Békési et al. (2017) for the
590 Pannonian Basin. They showed that regional fluid flow systems have major influence on the temperature field,
591 resulting in large model uncertainties. We established an a-priori conductivity profile for the carbonate platforms
592 to fit the temperature profile in the LTG-01 well. We allowed prior conductivities to vary in certain bounds in
593 order to obtain a satisfying fit with temperature measurements at shallower depth. Our approach results in
594 relatively high modeled temperatures at larger depth. These show a good correlation with the locations of the
595 carbonate platforms (Figure 8, 4-6 km depth) and could highlight potential target areas for deep geothermal
596 exploration. The application of a conductive model to convective areas has several limitations. For instance,
597 convective cells cannot be properly modeled with conduction, as their extent and geometry cannot be taken into
598 account. The pseudo-convective approach results in larger modeled temperatures throughout the whole
599 convective layer. However, the structure of hydrothermal convection is much more complex (e.g. Guillou-
600 Frottier et al., 2013). The temperature distribution inside convection cells is not homogenous: lower temperatures
601 are associated with downwellings, and warmer areas correspond to upwellings. Additionally, hydrothermal
602 convection is more likely to occur locally, and convective cells may extend beyond the carbonate platforms
603 (Lipsey et al., 2016). Therefore, our model overestimates temperatures at the depth of the carbonate platforms
604 without the presence of fluid convection and at downwelling zones. Also, the thermal effect of convection
605 beyond the platform areas cannot be captured. Our model is only able to indicate potential locations where
606 higher temperatures might be present. Successful development of the Dinantian carbonates requires site-specific
607 studies taking into account the local geometry of the carbonate platforms and incorporating convective heat
608 transfer.

609 It is important to note that the LTG-01 well is the only indication for potential convection in the platforms.
610 Another explanation of the thermal anomaly might be the large thermal conductivity contrast between the
611 Numerian and Westpalian sediments and the Dinantian carbonate platforms (Veldkamp and Hegen, 2020). Our
612 model with a modified thermal conductivity values aims for approximating fluid convection, but the modified
613 thermal conductivities could also account for the case of a strong thermal conductivity contrast. Without the
614 observations from this well, our modeling approach would have most likely been different, with less focus and
615 constraints on the carbonate formations. It demonstrates the need for deep exploration wells that can not only
616 provide more information on deep geological structures, layers, and reservoir properties, but also on the deep
617 thermal structure. The restricted amount of information available at larger depths, leads to a significant increase
618 in uncertainty with depth for our thermal models.

619 The previous temperature model of the onshore Netherlands was constructed by Bonté et al. (2012). We
620 incorporated their work in our study and we added several new aspects to the modeling. To improve our model
621 calibration results, we updated the temperature database with more recent temperature measurements, including
622 production temperatures from geothermal wells. We constructed our sedimentary layers based on the
623 sedimentary model of the onshore Netherlands (DGM-deep v4.0). Furthermore, we added new layers
624 corresponding to the Dinantian (Carboniferous) and older Palaeozoic sediments. By taking into account the
625 thermal effect of convection in the Dinantian carbonate platforms, we reproduced the thermal anomaly observed
626 in the LTG-01 well. However, our model only solves the heat equation in steady state, without taking into
627 account transient effects of vertical tectonic motions and paleo surface temperature fluctuations. Vertical
628 motions originate from sedimentation/erosion and large-scale deformations such as lithospheric stretching. Bonté
629 et al. (2012) incorporated vertical motions for the latest stage of basin evolution from 20 Ma until recent,
630 originating from the accumulation of sediments. Since large-scale lithospheric deformations with significant
631 temperature perturbations have no effect on the present-day temperatures in the Netherlands (major tectonism
632 associated with the stretching of the lithosphere and inversion took place over 100 My and ~65 My ago (e.g.
633 Van Wees et al., 2009), we concluded that a steady-state temperature model would suffice for the Netherlands.

634 Our model show a good correspondence with the German temperature maps (Agemar et al., 2012) along the
635 eastern border of the Netherlands between 2 and 4 km depth. Large temperature variations (up to ±10 °C) can be
636 observed in 1 to 3 km depth (Figure 8) due to the presence of the highly conductive evaporites within the
637 Zechstein Group (layer 8) mostly in the northern part of the country, where salt diapers are present (Geluk,
638 2005). The top of the salt layer is marked by high temperatures, for instance in the Friesland Platform,

639 Lauwerszee Trough, Groningen High and Lower Saxony Basin, whereas isotherms are depressed below the
640 highly conductive salts (e.g. Figure 10). The same thermal effect is observed in the westernmost part of the
641 North German Basin (Lower Saxony) (Agemar et al., 2012) and in the in the central Polish Basin (Zielinski et
642 al., 2012). Elevated temperatures above salt layers provide potential target areas for geothermal exploitation in
643 the northeastern part of the Netherlands (Daniilidis and Herber, 2017). Daniilidis and Herber (2017) show that
644 the thermal anomaly is not only dependent on the thickness of the salt layer, but the shape of the salt intrusion
645 also plays an important role. Detailed site-specific studies taking into account the local geology including the
646 potential for a suitable aquifer are necessary to exploit the geothermal potential of salt bodies in sedimentary
647 basin settings. Temperature anomalies attributed to the Silesian sediments with low thermal conductivity can
648 also be observed throughout the Netherlands. These sediments are predominantly shales with relatively high coal
649 content, resulting in an insulating thermal effect (e.g. Figure 10). Modeled temperatures above 3 km depth are
650 lower than average observed temperatures in the West Netherlands Basin, Roer Valley Graben, and Central
651 Netherlands Basin, in agreement with the earlier findings of Bonté et al. (2012). These pronounced negative
652 anomalies can be explained by the large thickness of the Silesian sediments. The Dinantian carbonate platforms
653 marked by high conductivity appear as positive temperature anomalies at larger depth. Additionally, the
654 carbonate platforms in the south are identified as areas with larger than average temperatures, except for the
655 Limburg High. The coldest areas below 3 km depth correspond to the Zeeland High and Limburg High and are
656 likely caused by the absence of a thick sedimentary cover on top of the highly conductive basement rocks.

657 Different horizontal mesh resolutions may influence the calculation of thermal properties, resulting in slight
658 variations in predicted temperatures (Figure 9). This effect is negligible in areas where the thermal field is
659 dominantly conductive and no steep temperature gradients are present (Figure 9). On the other hand, within the
660 highly conductive layers including the Dinantian carbonate platforms where convection is approximated by a
661 higher than normal thermal conductivity, modeled temperatures are dependent on the horizontal mesh resolution
662 (Figure 9). The posterior model with a finer horizontal discretization can better capture the variations in the input
663 geological model, providing more reliable results and an improved fit with measured temperatures where steep
664 gradients occur. We did not test different vertical resolution of the models. Kaiser et al. (2013) concluded that
665 horizontal mesh resolution has a more significant effect on modeled temperatures. They suggested that effects on
666 temperatures modeled with conduction are almost independent from mesh resolution, however, discrepancies
667 may occur at steep gradients or high thermal conductivity contrasts. Our models with a different horizontal
668 discretization agree with their findings. Since the thermal field of the onshore Netherlands is dominantly
669 conductive, we can conclude that both horizontal mesh resolutions are able to approximate the thermal field
670 sufficiently. On the other hand, at locations where fluid convection exists, discrepancies in modeled temperatures
671 may arise.

672 Calibrating the model with ES-MDA, reduces misfits of the prior model, although the variation in the data is not
673 entirely captured by the ensembles (Figure 11). The required variation within the measurements could be
674 reached by allowing more variation within the model parameters, especially in the shallower part of the model.
675 On the other hand, a larger variation within these thermal properties would not be realistic. We only allowed
676 unrealistic thermal conductivity values in the carbonate platforms and in the Limburg group (overlaying layer) in
677 order to approximate the thermal effect of convection in the deeply buried carbonates. For the rest of the layers,
678 we chose the scaling parameters to ensure that the thermal conductivities remain realistic. It was important
679 especially in the shallow part of the model, where large amounts of measurements are available, many of them
680 having errors up to ±15 °C. Allowing a wider scaling range would provide better fit with the temperature data,
681 although the predicted temperatures would vary significantly in a small spatial proximity, resulting in unrealistic
682 anomalies. We assume that the misfits are partly caused by transient effects or convective heat transfer. Fluid
683 flow along fault structures are commonly identified as a cause of misfits of conductive models (e.g. Freymark et
684 al., 2017). Both the prior and posterior models show a remarkable positive misfit at shallow depth: temperatures
685 are systematically overestimated at 1 and 2 km depth (Figure 11, Table 3). The most pronounced misfits are
686 observed in the shallowest depth interval (Table 3, 1000 m ± 400 m). We explain these misfits with the transient
687 thermal effect of the paleo-temperature fluctuations (e.g. Donders et al., 2009; Verweij et al., 2012). We
688 attempted to account for the thermal effect of recent glaciation by choosing a lower surface temperature as a
689 boundary condition, although we cannot entirely reproduce it with our steady-state model. Ter Voorde et al.
690 (2014) also concluded that the misfits with the steady-state thermal profile in shallow depth reflect a transient
691 condition inherited from past climate change. Alternatively, groundwater flows can also explain local anomalies
692 at shallow depth. Measurements errors are also partly responsible for misfits, especially at 1-2 km depth, where a
693 large number of data points are available in close spatial proximity (e.g. in the WNB, CNB-NHP border).

694 Systematic small under- or overestimates might be caused by boundary conditions and/or heat generation in
695 thick layers that have a larger lateral extent (e.g. upper crust or a sedimentary layer that is widespread across the
696 Netherlands. Other local misfits might be caused by uncertainties in model geometry, lithology mixtures (e.g.
697 thermal properties of the sedimentary layers), etc.

698 10. Conclusions

699 We established a 3D high-resolution subsurface temperature model of the onshore Netherlands. One of the most
700 important aspects of this study is the validation of the thermal model with 1507 temperature measurements. We
701 calibrated our model with temperature observations through inversion with ES-MDA. We took into
702 consideration both the data and model uncertainties by assuming a Gaussian distribution for measurement errors
703 and a triangular distribution for scaling the thermal properties. Misfits of the prior model are reduced through
704 the data assimilation procedure: the overall RMS, including all the measurements, decreases from a value of 0.95
705 °C for the prior model to 0.70 °C for the posterior model. It demonstrates the effectiveness of ES-MDA as a tool
706 for calibrating temperature models, supporting high-resolution external constraints. On the other hand, for areas
707 without temperature data available, especially in the deeper parts of the model, predicted temperatures are
708 strongly dependent on conceptual constraints. Therefore, a reliable geological model and reasonable thermal
709 properties are crucial as modelling input.

710 By taking into account the thermal effect of convection in the Dinantian carbonate platforms, we reproduced the
711 thermal anomaly observed in the LTG-01 well. Our model reveals areas with potential for hydrothermal
712 convection in the deep carbonate platforms. These locations can be suitable for deep geothermal development of
713 both electricity generation and direct heat uses due to the sufficiently high temperatures and inferred high
714 permeabilities that are required for convection. The temperature model has been incorporated into the updated
715 ThermoGIS project and is available online at thermogis.nl

716

721

722 Data availability

723 Temperature data that we use for the calibration of our model are available at the Netherlands Oil and Gas Portal
724 website (www.nlog.nl). The DGM-deep v4.0 geological model representing the main sedimentary units of the
725 Netherlands and used for our modeling input is published on www.nlog.nl. Our final temperature model is
726 available online at thermogis.nl.

727

728 References

729 Agemar, T., Schellschmidt, R., Schulz, R., 2012. Subsurface temperature distribution in Germany.
730 Geothermics 44, 65-77.
731 Artemieva, I.M., 2019. Lithosphere structure in Europe from thermal isostasy. Earth-Science Reviews
732 188, 454-468.
733 Batzle, M., Wang, Z., 1992. Seismic properties of pore fluids. Geophysics 57(11), 1396-1408.
734 Beglinger, S.E., van Wees, J.-D., Cloetingh, S., Doust, H., 2012. Tectonic subsidence history and
735 source-rock maturation in the Campos Basin, Brazil. Petroleum Geoscience 18(2), 153-172.
736 Békési, E., Lenkey, L., Limberger, J., Porkoláb, K., Balázs, A., Bonté, D., Vrijlandt, M., Horváth, F.,
737 Cloetingh, S., van Wees, J.-D., 2017. Subsurface temperature model of the Hungarian part of the
738 Pannonian Basin. Global and Planetary Change.
739 Bonté, D., Van Wees, J.-D., Verweij, J., 2012. Subsurface temperature of the onshore Netherlands:
740 new temperature dataset and modelling. Netherlands Journal of Geosciences 91(4), 491-515.

741 Boxem, T.P.A., 2010. Steady state 1D temperature modeling of the onshore Dutch subsurface.
742 Netherlands Institute of Applied Science TNO – National Geological Survey (Utrecht), p. 86 pp.

743 Breede, K., Dzebisashvili, K., Liu, X., Falcone, G., 2013. A systematic review of enhanced (or
744 engineered) geothermal systems: past, present and future. Geothermal Energy 1(1), 4.

745 Chapman, D., 1986. Thermal gradients in the continental crust. Geological Society, London, Special
746 Publications 24(1), 63-70.

747 Cloetingh, S., Van Wees, J.D., Ziegler, P., Lenkey, L., Beekman, F., Tesauro, M., Förster, A., Norden, B.,
748 Kaban, M., Hardebol, N., 2010. Lithosphere tectonics and thermo-mechanical properties: an
749 integrated modelling approach for Enhanced Geothermal Systems exploration in Europe. Earth-
750 Science Reviews 102(3-4), 159-206.

751 Daniilidis, A., Herber, R., 2017. Salt intrusions providing a new geothermal exploration target for
752 higher energy recovery at shallower depths. Energy 118, 658-670.

753 De Jager, J., 2007. Geological development. Geology of the Netherlands. Royal Netherlands Academy
754 of Arts and Sciences, Amsterdam 5, 26.

755 Donders, T., Weijers, J., Munsterman, D., Kloosterboer-van Hoeve, M., Buckles, L., Pancost, R.,
756 Schouten, S., Damsté, J.S., Brinkhuis, H., 2009. Strong climate coupling of terrestrial and marine
757 environments in the Miocene of northwest Europe. Earth and Planetary Science Letters 281(3-4),
758 215-225.

759 Doornenbal, H., Stevenson, A., 2010. Petroleum geological atlas of the Southern Permian Basin area.
760 EAGE.

761 Duin, E., Doornenbal, J., Rijkers, R., Verbeek, J., Wong, T.E., 2006. Subsurface structure of the
762 Netherlands-results of recent onshore and offshore mapping. Netherlands Journal of Geosciences
763 85(4), 245.

764 Emerick, A.A., Reynolds, A.C., 2013a. Ensemble smoother with multiple data assimilation. Computers
765 & Geosciences 55, 3-15.

766 Emerick, A.A., Reynolds, A.C., 2013b. Investigation of the sampling performance of ensemble-based
767 methods with a simple reservoir model. Computational Geosciences 17(2), 325-350.

768 Fokker, P., Wassing, B., van Leijen, F., Hanssen, R., Nieuwland, D., 2016. Application of an ensemble
769 smoother with multiple data assimilation to the Bergermeer gas field, using PS-InSAR. Geomechanics
770 for Energy and the Environment 5, 16-28.

771 Freymark, J., Sippel, J., Scheck-Wenderoth, M., Bär, K., Stiller, M., Fritsche, J.-G., Kracht, M., 2017.
772 The deep thermal field of the Upper Rhine Graben. Tectonophysics 694, 114-129.

773 Geluk, M., Wong, T., Batjes, D., De Jager, J., 2007. Permian. Geology of the Netherlands, 63-83.

774 Geluk, M.C., 2005. Stratigraphy and tectonics of Permo-Triassic basins in the Netherlands and
775 surrounding areas. Utrecht University.

776 Goutorbe, B., Lucazeau, F., Bonneville, A., 2007. Comparison of several BHT correction methods: a
777 case study on an Australian data set. Geophysical Journal International 170(2), 913-922.

778 Grunnberg, L., 1970. Properties of seawater concentrations, Third International Symposium on Fresh
779 Water from the Sea. Dubrovnik.

780 Guillou-Frottier, L., Carré, C., Bourgine, B., Bouchot, V., Genter, A., 2013. Structure of hydrothermal
781 convection in the Upper Rhine Graben as inferred from corrected temperature data and basin-scale
782 numerical models. Journal of Volcanology and Geothermal Research 256, 29-49.

783 Haenel, R., 1980. Atlas of subsurface temperatures in the European Community. Commission of the
784 European Communities, Directorate-General Scientific and ….

785 Haenel, R., Staroste, E., 1988. Atlas of geothermal resources in the European Community, Austria and
786 Switzerland. ESC.

787 Hantschel, T., Kauerauf, A.I., 2009. Fundamentals of basin and petroleum systems modeling. Springer
788 Science & Business Media.

789 Horton, C., Rogers Jr, F., 1945. Convection currents in a porous medium. Journal of Applied Physics
790 16(6), 367-370.

791 Hurter, S., Haenel, R., 2002. Atlas of geothermal resources in Europe.

792 Hurtig, E., Cermak, V., Haenel, R., Zui, V., 1992. Geothermal atlas of Europe.

Kaiser, B.O., Cacace, M., Scheck-Wenderoth, M., 2013. 3D coupled fluid and heat transport simulations of the Northeast German Basin and their sensitivity to the spatial discretization: different sensitivities for different mechanisms of heat transport. Environmental earth sciences 70(8), 3643-3659.

Kalkman, A., Veldkamp, H., Boxem, T., Koornneef, J., Halter, M., 2016. Ultra-Diepe Geothermie - Casus Almere en Barendrecht. Netherlands Institute of Applied Science TNO – National Geological Survey.

Kombrink, H., 2008. The Carboniferous of the Netherlands and surrounding areas; a basin analysis. Geologica Ultraiectina (294). Departement Aardwetenschappen.

Kombrink, H., Doornenbal, J., Duin, E., Den Dulk, M., Ten Veen, J., Witmans, N., 2012. New insights into the geological structure of the Netherlands; results of a detailed mapping project. Netherlands Journal of Geosciences 91(4), 419-446.

Lapwood, E., 1948. Convection of a fluid in a porous medium, Mathematical Proceedings of the Cambridge Philosophical Society. Cambridge University Press, pp. 508-521.

Limberger, J., Calcagno, P., Manzella, A., Trumpy, E., Boxem, T., Pluymaekers, M., van Wees, J.-D., 2014. Assessing the prospective resource base for enhanced geothermal systems in Europe. Geothermal Energy Science 2(1), 55-71.

Limberger, J., van Wees, J.-D., Tesauro, M., Smit, J., Bonté, D., Békési, E., Pluymaekers, M., Struijk, M., Vrijlandt, M., Beekman, F., 2018. Refining the thermal structure of the European lithosphere by inversion of subsurface temperature data. Global and Planetary Change.

Lipsey, L., Pluymaekers, M., Goldberg, T., van Oversteeg, K., Ghazaryan, L., Cloetingh, S., van Wees, J.-D., 2016. Numerical modelling of thermal convection in the Luttelgeest carbonate platform, the Netherlands. Geothermics 64, 135-151.

Luijendijk, E., Ter Voorde, M., Van Balen, R., Verweij, H., Simmelink, E., 2011. Thermal state of the Roer Valley Graben, part of the European cenozoic rift system. Basin Research 23(1), 65-82.

Moeck, I., Beardsmore, G., 2014. A new 'geothermal play type'catalog: Streamlining exploration decision making, Proceedings of the Thirty-Ninth Workshop on Geothermal Reservoir Engineering, Stanford University, Stanford, California.

Pharaoh, T., Dusar, M., Geluk, M., Kockel, F., Krawczyk, C., Krzywiec, P., Scheck-Wenderoth, M., Thybo, H., Vejbæk, O., Van Wees, J.D., 2010. Tectonic evolution, Petroleum geological atlas of the Southern Permian Basin area. EAGE Publications bv (Houten), pp. 25-57.

Reijmer, J.J., Johan, H., Jaarsma, B., Boots, R., 2017. Seismic stratigraphy of Dinantian carbonates in the southern Netherlands and northern Belgium. Netherlands Journal of Geosciences 96(4), 353-379.

Rijkers, R., Van Doorn, T.H., 1997. Atlas of Geothermal resources in the European Community, the Netherlands. Netherlands Institute of Applied Geoscience TNO–National Geological Survey. Report 97-24-A.

Rühaak, W., 2015. 3-D interpolation of subsurface temperature data with measurement error using kriging. Environmental earth sciences 73(4), 1893-1900.

Saeid, S., Al-Khoury, R., Barends, F., 2013. An efficient computational model for deep low-enthalpy geothermal systems. Computers & geosciences 51, 400-409.

Schatz, J.F., Simmons, G., 1972. Thermal conductivity of earth materials at high temperatures. Journal of Geophysical Research 77(35), 6966-6983.

Schmeling, H., Marquart, G., 2014. A scaling law for approximating porous hydrothermal convection by an equivalent thermal conductivity: theory and application to the cooling oceanic lithosphere. Geophysical Journal International 197(2), 645-664.

Sekiguchi, K., 1984. A method for determining terrestrial heat flow in oil basinal areas. Tectonophysics 103(1), 67-79.

Smit, J., van Wees, J.-D., Cloetingh, S., 2018. Early Carboniferous extension in East Avalonia: 350 My record of lithospheric memory. Marine and Petroleum Geology 92, 1010-1027.

Ten Veen, J., Van Gessel, S., Den Dulk, M., 2012. Thin-and thick-skinned salt tectonics in the Netherlands; a quantitative approach. Netherlands Journal of Geosciences 91(4), 447-464.

844 Ter Voorde, M., Van Balen, R., Luijendijk, E., Kooi, H., 2014. Weichselian and Holocene climate history
845 reflected in temperatures in the upper crust of the Netherlands. Netherlands Journal of Geosciences
846 93(3), 107-117.
847 Tesauro, M., Kaban, M.K., Cloetingh, S.A., 2008. EuCRUST-07: A new reference model for the
848 European crust. Geophysical Research Letters 35(5).
849 Tesauro, M., Kaban, M.K., Cloetingh, S.A., 2009. A new thermal and rheological model of the
850 European lithosphere. Tectonophysics 476(3), 478-495.
851 Van Adrichem Boogaert, H., Kouwe, W., 1993. Stratigraphic nomenclature of the Netherlands,
852 revision and update by RGD and NOGEPA: Mededelingen Rijks Geologische Dienst, v. 50.
853 Van Hulten, F., Poty, E., 2008. Geological factors controlling Early Carboniferous carbonate platform
854 development in the Netherlands. Geological Journal 43(2-3), 175-196.
855 Van Oversteeg, K., Lipsey, L., Pluymaekers, M., Van Wees, J.D., Fokker, P.A., Spiers, C., 2014. Fracture
856 permeability assessment in deeply buried carbonates and implications for enhanced geothermal
857 systems: inferences from a detailed well study at Luttelgeest-01, The Netherlands, Proceedings
858 Thirty-Eighth Workshop on Geothermal Reservoir Engineering, Stanford University, Stanford,
859 California.
860 Van Wees, J.-D., Kronimus, A., Van Putten, M., Pluymaekers, M., Mijnlieff, H., Van Hooff, P., Obdam,
861 A., Kramers, L., 2012. Geothermal aquifer performance assessment for direct heat production–
862 Methodology and application to Rotliegend aquifers. Netherlands Journal of Geosciences 91(4), 651-
863 665.
864 Van Wees, J.-D., Stephenson, R., Ziegler, P., Bayer, U., McCann, T., Dadlez, R., Gaupp, R., Narkiewicz,
865 M., Bitzer, F., Scheck, M., 2000. On the origin of the southern Permian Basin, Central Europe. Marine
866 and Petroleum Geology 17(1), 43-59.
867 Van Wees, J., Van Bergen, F., David, P., Nepveu, M., Beekman, F., Cloetingh, S., Bonté, D., 2009.
868 Probabilistic tectonic heat flow modeling for basin maturation: Assessment method and applications.
869 Marine and Petroleum Geology 26(4), 536-551.
870 Veldkamp, J.G., Hegen, D., 2020. Temperature modelling of the Dutch subsurface at the depth of the
871 Dinantian. Netherlands Organisation for Applied Scientific Research TNO.
872 Verweij, H.M., Echternach, M.S.C., Witmans, N., Fattah, R.A., 2012. Reconstruction of basal heat flow,
873 surface temperature, source rock maturity, and hydrocarbon generation in salt-dominated Dutch
874 Basins.
875 Verweij, J.M., 2003. Fluid flow systems analysis on geological time scale in onshore and offshore
876 Netherlands, with special reference to the Broad Fourteens Basin. Vrije Universiteit (Amsterdam), p.
877 278.
878 Willems, C., 2017. Doublet deployment strategies for geothermal Hot Sedimentary Aquifer
879 exploitation: Application to the Lower Cretaceous Nieuwerkerk Formation in the West Netherlands
880 Basin.
881 Wong, T.E., Batjes, D.A., de Jager, J., 2007. Geology of the Netherlands. Edita-the Publishing House of
882 the Royal.
883 Xu, Y., Shankland, T.J., Linhardt, S., Rubie, D.C., Langenhorst, F., Klasinski, K., 2004. Thermal diffusivity
884 and conductivity of olivine, wadsleyite and ringwoodite to 20 GPa and 1373 K. Physics of the Earth
885 and Planetary Interiors 143, 321-336.
886 Ziegler, P.A., 1990. Geological atlas of western and central Europe. Geological Society of London.
887 Zielinski, G.W., Poprawa, P., Szewczyk, J., Grotek, I., Kiersnowski, H., Zielinski, R.L., 2012. Thermal
888 effects of Zechstein salt and the Early to Middle Jurassic hydrothermal event in the central Polish
889 Basin. AAPG bulletin 96(10), 1981-1996.

890

891